

Statistics of Dark Matter Substructure: III. Halo-to-Halo Variance

Fangzhou Jiang^{*} & Frank C. van den Bosch

Department of Astronomy, Yale University, New Haven, CT 06511, USA

ABSTRACT

We present a study of unprecedented statistical power regarding the halo-to-halo variance of dark matter substructure. Using a combination of N -body simulations and a semi-analytical model, we investigate the variance in subhalo mass fractions and subhalo occupation numbers, with an emphasis on how these statistics scale with halo formation time. We demonstrate that the subhalo mass fraction, f_{sub} , is mainly a function of halo formation time, with earlier forming haloes having less substructure. At fixed formation redshift, the average subhalo mass fraction is virtually independent of halo mass, and the mass dependence of f_{sub} is therefore mainly a manifestation of more massive haloes assembling later. We compare observational constraints on f_{sub} from gravitational lensing to our model predictions and simulation results. Although the inferred f_{sub} are substantially higher than the median Λ CDM predictions, they fall within the 95th percentile due to halo-to-halo variance. We show that the halo occupation distributions of subhaloes do not follow Poisson statistics; whereas $P(N|M)$ is super-Poissonian for large $\langle N \rangle$, a result that is well established, it becomes sub-Poissonian for $\langle N \rangle \lesssim 2$. We show that ignoring this non-Poissonity results in systematic errors of the predicted clustering of galaxies of a few percent, and with a complicated scale- and luminosity-dependence. Haloes that assemble earlier have $P(N|M)$ that are closer to a Poisson distribution, suggesting that the dynamical evolution of subhaloes drives the statistics towards Poissonian. However, contrary to a recent claim, the non-Poissonity of subhalo occupation statistics does not vanish by selecting haloes with fixed mass and fixed formation redshift. Finally, we use subhalo occupation statistics to put loose constraints on the mass and formation redshift, z_f , of the Milky Way halo. Using observational constraints on the maximum circular velocities of the three most massive satellite galaxies in the Milky Way, we infer that $0.25 < M_{\text{vir}}/10^{12} h^{-1} M_{\odot} < 1.4$ and $0.1 < z_f < 1.4$ at 90% confidence level.

Key words: methods: analytical — methods: statistical — galaxies: haloes — dark matter

1 INTRODUCTION

In the hierarchical Λ +CDM structure formation paradigm, dark matter haloes contain subhaloes, which are the remnants of halos that have been accreted by their host halo over cosmic time, and have survived tidal destruction. Since the assembly history of a dark matter halo depends on halo mass, cosmology, and its large scale environment, so do the statistics of subhaloes. As a consequence, the large halo-to-halo variance in halo assembly histories gives rise to a very significant halo-to-halo variance in the substructure content of dark matter haloes, even at a fixed halo mass.

An accurate knowledge of this halo-to-halo variance has

numerous applications. For example, the severity of the ‘too-big-to-fail’ problem (Boylan-Kolchin et al. 2011) strongly depends on the halo-to-halo variance of the abundance and internal densities of massive subhaloes (e.g., Purcell & Zentner 2012; Jiang & van den Bosch 2015). Second, whether or not the gamma-ray excess at $\sim 2\text{GeV}$ from the Galactic Center (e.g., Calore et al. 2015) is attributable to dark matter self-annihilation depends on the abundance of subhaloes along the line-of-sight (e.g., Anderhalden et al. 2013; Correa et al. 2015), which is subject to large uncertainties arising from the halo-to-halo variance. Third, the demographics of satellite galaxies is directly related to that of subhaloes (e.g., Kravtsov et al. 2004). As a consequence, models for the halo occupation statistics of galaxies, which are used to interpret galaxy clustering measurements, are guided by the occupation statistics of subhaloes. As we will demon-

^{*} E-mail:fangzhou.jiang@yale.edu

strate, standard (oversimplified) assumptions regarding the functional form of the halo-to-halo variance can result in significant errors in the predicted two-point correlation functions of satellite galaxies. And finally, a proper treatment of the halo-to-halo variance is of paramount importance when comparing subhalo masses inferred from gravitational lensing with CDM predictions (e.g., Vegetti et al. 2014; Okabe et al. 2014; Xu et al. 2015).

In this paper, we use a combination of cosmological N -body simulations and a semi-analytical model of halo assembly and subhalo evolution, to study the halo-to-halo variance of subhalo demographics at unprecedented statistical power. The semi-analytical model is devised to quickly generate large ensembles of subhalo populations at high mass resolution for a broad range of host halo mass and cosmology. It is described in detail in Jiang & van den Bosch (2016, Paper I), and its accuracy has been tested against multiple simulations in van den Bosch & Jiang (2016, Paper II). In particular, as shown in Jiang & van den Bosch (2015), the model accurately reproduces the halo-to-halo variance in subhalo mass and velocity functions, and is therefore ideally suited for this study, to complement cosmological N -body simulations where they have limiting statistical power. This happens both at the massive end, where the abundance of host haloes is insufficient to accurately probe the halo-to-halo variance, and at the low mass end, where the limiting mass resolution only allows the study of subhalo statistics over a tiny dynamic range in mass.

The paper is organized as follows. In §2 we briefly describe the semi-analytical model and the various N -body simulations used. In §3 we demonstrate that the subhalo mass fraction is basically a function of halo formation time, and we compare constraints on the subhalo mass fraction obtained using gravitational lensing measurements to predictions from our model and from a variety of numerical simulations. In §4 we focus on the halo occupation distribution (HOD) of dark matter subhaloes, $P(N|M)$, which expresses the probability that a host halo of mass M contains N subhaloes above a given mass limit. We demonstrate that $P(N|M)$ deviates strongly, and in a complicated way, from a Poisson distribution, and discuss the implications for HOD models of galaxy clustering. We also address the dependence of the magnitude of the non-Poissonity on halo formation redshift. Finally, in §5, we use the occupation statistics of massive subhaloes to put constraints on the mass and formation time of the Milky Way halo. We summarize our findings in §6.

Throughout, we use lower- and upper-case letters to indicate subhalo and host halo properties, respectively. For example, m and v_{\max} represent the mass and maximum circular velocity of a subhalo, while M and V_{\max} correspond to the same quantities but for a host halo. We use ψ to either denote subhalo mass in units of the present-day host halo virial mass, m/M_0 , or the subhalo maximum circular velocity in units of the present-day host halo virial velocity, $v_{\max}/V_{\text{vir},0}$. Throughout, we define halo formation time as the earliest redshift (z_f) by which a halo has assembled half of its present-day mass.

2 METHOD

2.1 N -body Simulations

The main simulations that we use in this study are the Bolshoi (Klypin et al. 2011) and MultiDark (Prada et al. 2012) simulations. Both follow the evolution of 2048^3 dark matter particles using the Adaptive Refinement Tree (ART) code (Kravtsov, Klypin & Khokhlov 1997) in a flat Λ CDM cosmology with parameters $(\Omega_{\text{m},0}, \Omega_{\Lambda,0}, \Omega_{\text{b},0}, h, \sigma_8, n_s) = (0.27, 0.73, 0.047, 0.7, 0.82, 0.95)$. Bolshoi has a particle mass of $m_p = 1.35 \times 10^8 h^{-1} M_\odot$ and a box of size $250 h^{-1} \text{Mpc}$, while MultiDark has a particle mass of $m_p = 8.7 \times 10^9 h^{-1} M_\odot$ and a box of size $1000 h^{-1} \text{Mpc}$. As shown in Paper II, due to the limited mass resolution, the evolved subhalo mass functions become incomplete below 50 particles, which corresponds to a mass scale of $M_{\text{res}} = 10^{9.83} h^{-1} M_\odot$ and $10^{11.64} h^{-1} M_\odot$ for Bolshoi and MultiDark, respectively.

We also use published results or publicly available data from several suites of zoom-in simulations, including Rhapsody (Wu et al. 2013), ELVIS (Garrison-Kimmel et al. 2014a), Phoenix (Gao et al. 2012), Aquarius (Springel et al. 2008), and COCO (Bose et al. 2016). These are obtained by re-simulating specific haloes or sub-volumes, extracted from medium-resolution cosmological volumes, at much higher resolution. Details of all simulations used throughout this work are summarized in Table 2.1, and we refer interested readers to the original papers for details.

Haloes and subhaloes in Bolshoi, MultiDark, Rhapsody, and ELVIS are identified using the ROCKSTAR halo finder (Behroozi et al. 2013a,b), while COCO, Phoenix and Aquarius results are obtained using SUBFIND (Springel et al. 2001). ROCKSTAR is a phase-space halo finder, which uses adaptive, hierarchical refinement of friends-of-friends groups in six phase-space dimensions and one time dimension. SUBFIND, on the other hand, only relies on information in configuration-space. As discussed in Paper II, SUBFIND has a tendency to underestimate the masses of subhaloes close to the center of the host halo, which has an appreciable impact on the massive end of the subhalo mass function.

Halo mass is defined as the mass enclosed in a sphere with an average density of Δ times the critical density of the Universe. For Bolshoi, MultiDark, Rhapsody, and ELVIS $\Delta = \Delta_{\text{vir}} \sim 100$, with Δ_{vir} given by the fitting function of Bryan & Norman (1998), while the halo catalogs of COCO, Phoenix, and Aquarius are based on $\Delta = 200$. When needed, we convert M_{200} to M_{vir} using the average concentration mass relation of Maccio et al. (2008).

2.2 Semi-analytical model

In addition to the N -body simulations described above, we also use the semi-analytical model of substructure evolution developed in Jiang & van den Bosch (2016). Here we briefly describe the model, and refer interested readers to Paper I for more details. The model constructs halo merger trees using the algorithm developed by Parkinson et al. (2008), uses simple semi-analytical descriptions to evolve subhalo mass and structure, considers the entire hierarchy of substructure, and includes an empirical treatment of subhalo disruption. As shown in Jiang & van den Bosch (2014), the merger statistics from the Parkinson et al. algorithm are in

Table 1. Numerical Simulations used in this Paper

Simulation	$\Omega_{m,0}$	$\Omega_{\Lambda,0}$	$\Omega_{b,0}$	σ_8	n_s	h	L_{box} $h^{-1}\text{Mpc}$	N_p	m_p $h^{-1}M_{\odot}$	N_{halo}	M_{halo} $h^{-1}M_{\odot}$	Reference
Bolshoi	0.27	0.73	0.047	0.82	0.95	0.70	250	2048 ³	1.35×10^8	–	–	Klypin et al. (2011)
MultiDark	0.27	0.73	0.047	0.82	0.95	0.70	1000	2048 ³	8.7×10^9	–	–	Prada et al. (2012)
Rhapsody	0.25	0.75	0.04	0.8	1.0	0.70	–	8192 ³	1.3×10^8	96	$M_{\text{vir}} = 10^{14.8 \pm 0.05}$	Wu et al. (2013)
ELVIS	0.266	0.734	0.045	0.801	0.963	0.70	–	–	1.35×10^5	48	$M_{\text{vir}} = 10^{12.08 \pm 0.23}$	Garrison-Kimmel et al. (2014a)
COCO	0.272	0.728	0.045	0.81	0.967	0.704	17.4	1.3×10^{10}	1.14×10^5	–	–	Bose et al. (2016)
Phoenix	0.25	0.75	0.045	0.9	1.0	0.73	–	–	6.4×10^5	9	$M_{200} = 10^{15.0 \pm 0.3}$	Gao et al. (2012)
Aquarius	0.25	0.75	0.045	0.9	1.0	0.73	–	–	1.7×10^3	6	$M_{200} = 10^{11.93 \pm 0.18}$	Springel et al. (2008)

Note: COCO re-simulates a volume which approximates a sphere of radius $17.4 h^{-1}\text{Mpc}$ at the present time, extracted from a parent volume of $70.4 h^{-1}\text{Mpc}$. The other zoom-in simulations re-simulate individual haloes rather than a coherent sub-volume. We only focus on the COCO result for haloes with $M_{50} = 10^{12.25 \pm 0.25} h^{-1}M_{\odot}$.

excellent agreement with those from numerical simulations. Throughout this paper, we adopt the Bolshoi cosmology for the model, and we have verified that changing the cosmological parameters to any of the other cosmologies listed in Table 1 only results in very small differences (cf., Paper II and Dooley et al. 2014).

The mass of a subhalo is evolved using an orbit-averaged mass loss rate, $\dot{m} = f[m(t), M(t)]$, which takes a functional form that is motivated by a simple toy model of tidal stripping and has two free parameters: one determines the amplitude and the other controls the m/M -dependence. For each subhalo, the amplitude is drawn from a log-normal distribution that accounts for the scatter in orbital energies, orbital angular momenta and orbital phases.

The maximum circular velocity, v_{max} , and the corresponding radius, r_{max} , of a subhalo are computed using the empirical relations of Peñarrubia et al. (2010), $v_{\text{max}} = g_1(v_{\text{acc}}, m/m_{\text{acc}})$ and $r_{\text{max}} = g_2(r_{\text{acc}}, m/m_{\text{acc}})$. Note that v_{acc} and r_{acc} represent the v_{max} and r_{max} of a subhalo at accretion, which are computed by assuming an Navarro, Frenk & White (1997, NFW hereafter) density profile with a concentration $c(m_{\text{acc}}, t_{\text{acc}})$. The latter is determined from the mass assembly history of the subhalo progenitor prior to accretion using the model of Zhao et al. (2009). As such, the scatter in the merger histories of subhalo progenitors is imprinted in the structure of the evolved subhaloes. It turns out that the model prediction for the joint distribution of v_{max} and r_{max} of evolved subhaloes is indistinguishable from that in high-resolution simulations (see Jiang & van den Bosch 2015).

Following Taylor & Babul (2004), we consider a subhalo disrupted once its mass, $m(t)$, drops below a critical value $m_{\text{acc}}(< f_{\text{dis}} r_{\text{s,acc}})$, i.e., the mass enclosed at accretion within a radius that is f_{dis} times the NFW scale radius at accretion ($r_{\text{s,acc}}$). Like the mass loss rate, the critical mass also varies from one subhalo to another: for each subhalo, we draw a value for f_{dis} from a log-normal distribution that approximates the f_{dis} distribution of disrupting subhaloes in the Bolshoi simulation. Subhalo disruption is an indispensable ingredient of the model. As discussed in Paper I, one can construct a model without disruption that perfectly fits the evolved subhalo mass function (by enhancing the mass loss rates), but such a model predicts retained mass frac-

tions, m/m_{acc} , that are much lower than what is found in the simulation.

The advantage of the model is that it is extremely fast, which makes it useful to complement numerical simulations where they have limiting statistical power. For example, the Bolshoi simulation resolves the substructure in cluster-sized haloes ($M_0 \simeq 10^{14.5-15.0} h^{-1}M_{\odot}$) all the way down to $\sim 10^{-4.5} M_0$. However, because the Bolshoi simulation only covers $\sim 0.16 h^{-3} \text{Gpc}^3$, the actual number of cluster-sized haloes is too small for a reliable statistical analysis. The larger volume of the MultiDark simulation results in a much larger number of massive host haloes, but their subhaloes can only be resolved down to $\sim 10^{-3} M_0$. With the semi-analytical model, on the other hand, it is trivial to simulate thousands of massive host haloes with a mass resolution of $10^{-5} M_0$ in a matter of hours. As an example, Jiang & van den Bosch (2015) used the semi-analytical model to simulate tens of thousands of Milky-Way size host haloes with a mass resolution of $10^{-5} M_0$. For comparison, although the Bolshoi simulation contains hundreds of thousands of such Milky-way sized host haloes, it only resolves their substructure down to $\sim 10^{-2} M_0$.

2.2.1 The Prevalence of Subhalo Disruption

Tidal stripping and impulsive encounters with the host halo and with other subhaloes may ultimately result in the complete disruption of a subhalo. Subhalo disruption is prevalent in numerical simulations, to the extent that roughly half of all subhaloes ever accreted has been disrupted by $z = 0$ (e.g., Han et al. 2016; Paper I). To make this more quantitative, we use the semi-analytical model described in §2.2 above to construct 5000 model realizations of a host halo with mass $M_0 = 10^{13.5} h^{-1}M_{\odot}$ [†]. We compute the fraction of subhaloes that survive to the present day as a function of their mass and redshift at accretion. Results are shown in Fig. 1, where the thick, black line indicates the surviving fraction of all subhaloes with $m_{\text{acc}}/M_0 > 10^{-4}$ as a function of their accretion redshift. As is evident, less than 40% (10%) of subhaloes

[†] Results for other host halo masses are very similar

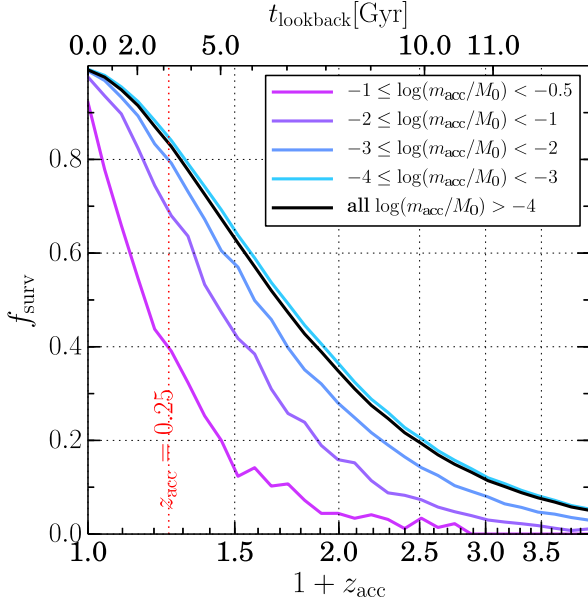


Figure 1. The surviving fraction of subhaloes as function of accretion redshift, z_{acc} , for subhaloes with different masses at accretion, m_{acc} , in host haloes with $M_0 = 10^{13.5} h^{-1} M_{\odot}$ (we have verified that the results show little dependence on host halo mass). Coloured lines indicate different bins in $\log(m_{\text{acc}}/M_0)$, as indicated, while the black line represents all subhaloes with $m_{\text{acc}} > 10^{-4} M_0$. The vertical, red dotted line at $z_{\text{acc}} = 0.25$ indicates the average accretion redshift for subhaloes that are currently at their first apo-center.

accreted at $z_{\text{acc}} = 1$ (2) survive to the present day. The colored lines indicate the surviving fractions among subhaloes in different bins of m_{acc}/M_0 (as indicated). There is a clear tendency for more massive subhaloes to undergo more efficient disruption. As many as 80% (95%) of all subhaloes with $m_{\text{acc}} > 0.01 M_0$ ($m_{\text{acc}} > 0.1 M_0$) have been disrupted since $z_{\text{acc}} = 1$. The average accretion redshift of subhaloes which have just completed their first orbit, and are currently at their apo-centers, is $z_{\text{acc}} \sim 0.25$ (van den Bosch et al. 2016). Based on this, we estimate from Fig.1 that $\sim 20\%$ of subhaloes with $m_{\text{acc}} > 10^{-4} M_0$ have been disrupted during their first orbital period. This fraction increases to 30% and 60% for subhaloes with $0.01 \leq m_{\text{acc}} < 0.1 M_0$, and $m_{\text{acc}} \geq 0.1 M_0$, respectively.

We caution that the efficiency of subhalo disruption depicted in Fig.1 is based on the model, which is tuned to reproduce subhalo evolution in the Bolshoi simulation. It is not yet clear to what extent subhalo disruption is due to numerical artifacts as opposed to the physical impact of tidal stripping and heating. Recall that it wasn't until the end of the 1990's that numerical simulations started to reach sufficient mass and force resolution to resolve a surviving population of subhaloes (e.g., Moore, Katz & Lake 1996; Tormen, Bouchet & White 1997; Ghigna et al. 1998; Klypin et al. 1999). And even today, the limiting mass and force resolution of numerical simulations may well result in a continued overmerging of substructure, especially near the centers of their host haloes. We will address the issue of nu-

merical disruption in more detail in a separate study (van den Bosch, in prep.). For now, it is important to be aware that the results presented here are only as accurate as the simulations used.

3 HALO-TO-HALO VARIANCE OF THE SUBHALO MASS FRACTION

We now use our model and the simulations listed in Table 1 to investigate the halo-to-halo variance in the subhalo mass fraction, which we define as

$$f_{\text{sub}}(\geq \psi) = \frac{1}{M_0} \sum_i m_i \Theta(\psi_i - \psi) = \int_{\psi}^1 \frac{dN}{d \ln \psi'} d\psi'. \quad (1)$$

Here \sum_i indicates summation over all subhaloes, $\Theta(x)$ is the Heaviside step function, ψ is shorthand notation for m/M_0 , and $dN/d \ln \psi$ is the subhalo mass function. Throughout this section, we consider a lower limit of $\psi = 10^{-4}$ [i.e., $f_{\text{sub}} = f_{\text{sub}}(\geq 10^{-4})$], unless stated otherwise.

As discussed in detail in Paper I, the subhalo mass fraction is the outcome of the competition between the accretion of new subhaloes and the dynamical evolution (tidal stripping and disruption) of existing subhaloes. At $z \sim 0$, the mass-loss timescale of subhaloes is of the order of the dynamical time ($\sim 2 \text{Gyr}$) and scales with redshift as $(1+z)^{-3/2}$ (e.g., Paper I). The time scale for the accretion of subhaloes is equivalent to the time scale of halo mass assembly, and is of the order of $M/\dot{M} \sim 10 \text{Gyr}$, with a similar redshift scaling at low z (e.g., McBride et al. 2009). Hence, at the present day most host haloes are in the regime of net subhalo mass loss (i.e., f_{sub} decreases with time). As a consequence, the subhalo mass fraction is strongly (anti-)correlated with the halo formation time (see Paper I), which is why it has been used as an indicator of the level of relaxedness of a halo (e.g., De Lucia et al. 2004; Shaw et al. 2006; Ludlow et al. 2013). In the context of flux-ratio anomalies of multiply-imaged quasars, the frequency and strength of anomalies scale with f_{sub} (Dalal & Kochanek 2002). Hence, a meaningful interpretation of flux-ratio anomalies requires a detailed understanding of the expected distribution of subhalo mass fractions.

In what follows, we first characterize the f_{sub} distribution as a function of host halo mass (§3.1), and then show that the halo mass dependence of the average mass fraction $\langle f_{\text{sub}} \rangle$ essentially reflects the fact that more massive haloes form later (§3.2). We consider both subhaloes and the subhaloes of subhaloes, which we refer to as first-order and second-order substructure, respectively. Finally, we compare the model predictions for f_{sub} with constraints inferred from gravitational lensing (§3.3).

3.1 Halo Mass Dependence

The left-hand panel of Fig.2 plots the subhalo mass fraction as a function of host halo mass. On average, f_{sub} increases with host halo mass, from $\sim 6\%$ at $M_0 = 10^{11} h^{-1} M_{\odot}$ to $\sim 17\%$ at $M_0 = 10^{15} h^{-1} M_{\odot}$. The relation can be approximated by

$$\log \langle f_{\text{sub}} \rangle = a + b \log \left(\frac{M_0}{10^{12} h^{-1} M_{\odot}} \right), \quad (2)$$

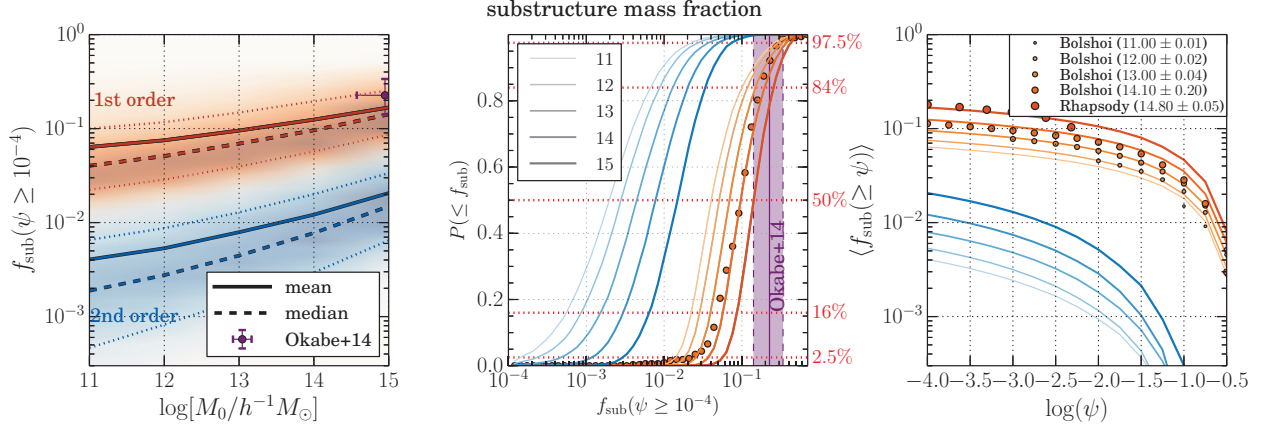


Figure 2. *Left-hand panel:* Mass fraction in present-day, surviving first-order (orange) and second-order (blue) subhaloes with $m \geq 10^{-4}M_0$, as a function of host halo mass. The solid, dashed and dotted lines represent the average, median, and the 16th and 84th percentiles respectively. The data point with errorbars is the weak lensing measurement of the subhalo mass fraction in the Coma cluster from Okabe et al. (2014). *Middle panel:* the cumulative distribution of subhalo mass fraction for five different host halo masses, as indicated. The vertical band indicates the Okabe et al. (2014) measurement. *Right-hand panel:* the average subhalo mass fraction, $\langle f_{\text{sub}}(\geq \psi) \rangle$ as a function of the mass threshold $\psi = m/M_0$.

with $(a, b) = (-1.12, 0.12)$ and $(-1.28, 0.13)$ good descriptions of the mean and median relations, respectively. For second-order subhaloes, the corresponding best-fit parameters are $(a, b) = (-2.26, 0.17)$ and $(-2.53, 0.22)$, respectively. Hence, the mass fraction of second-order subhaloes is roughly 10% of that of first-order subhaloes, which themselves make up roughly 10% of the mass of the host halo. This self-similarity is simply a manifestation of the self-similar nature of structure formation (cf. van den Bosch et al. 2014). Note that our halo mass definition is ‘inclusive’, i.e., the mass of a first-order subhalo includes the mass of all its second-order subhaloes.

There is a weak trend for the scatter in f_{sub} to be smaller for more massive haloes. In addition, for a given halo mass, the second-order f_{sub} has larger scatter than that of first-order subhaloes. We find that the f_{sub} distributions can be approximated by log-normal distributions with the mean $\log \langle f_{\text{sub}} \rangle$ given by Eq.(2), and the standard deviation given by

$$\sigma_{\log f_{\text{sub}}} = c + d \log \left(\frac{M_0}{10^{12} h^{-1} M_{\odot}} \right), \quad (3)$$

with $(c, d) = (0.26, -0.03)$ and $(0.5, -0.03)$ for first-order and second-order subhaloes, respectively.

The middle panel of Fig.2 plots the distributions of f_{sub} for host haloes with mass $M_0 = 10^{11}, 10^{12}, \dots, 10^{15} h^{-1} M_{\odot}$ (solid lines), based on 10,000 model realizations for each halo mass. In order to show that the model predictions are similar to the results from N -body simulations, we compare the f_{sub} distribution for model realizations of haloes with $M_0 = 10^{14} h^{-1} M_{\odot}$ to that for the 372 Bolshoi haloes with $M_0 = 10^{14.1 \pm 0.2} h^{-1} M_{\odot}$. This mass bin is chosen as a compromise between the need for a sufficient number of host haloes and the requirement that subhaloes are complete down to $m > 10^{-4} M_0$. The simulation results are in excellent agreement with the model predictions, although the former reveals a slightly more extended low- f_{sub} tail.

The right-hand panel of Fig.2 plots the average mass fraction, $\langle f_{\text{sub}}(\geq \psi) \rangle$, as a function of threshold mass, ψ .

From $\psi = 10^{-2}$ to 10^{-4} , the average mass fraction in first-order (second-order) subhaloes increases by a factor of ~ 2 (~ 4). We compare the average, first-order subhalo mass fraction, $\langle f_{\text{sub}}(\geq \psi) \rangle$, with that from numerical simulations. As before, the model predictions are based on 10,000 realizations of haloes with $M_0 = 10^{11}, 10^{12}, \dots, 10^{15} h^{-1} M_{\odot}$. The simulation results are based on the 16969, 4786, 1138, and 372 haloes with $M_0 = 10^{11 \pm 0.01}, 10^{12 \pm 0.02}, 10^{13 \pm 0.04}$, and $10^{14.1 \pm 0.2} h^{-1} M_{\odot}$ from the Bolshoi simulation, and the 96 haloes with $M_0 = 10^{14.8 \pm 0.05} h^{-1} M_{\odot}$ in the Rhapsody zoom-in suites, respectively. Good agreement is achieved for all the mass scales.

In a recent study, Okabe et al. (2014) used weak gravitational lensing to measure the mass of subhaloes in the Coma cluster. Adopting a host halo mass of $M_0 = 8.92_{-5.17}^{+20.05} \times 10^{14} h^{-1} M_{\odot}$ (Okabe et al. 2010) they infer a subhalo mass fraction $f_{\text{sub}}(> 10^{-3}) = 0.226_{-0.085}^{+0.111}$. This measurement is indicated as a purple data point in the left-hand panel and as a purple vertical band in the middle panel of Fig.2[‡]. As is evident, the Okabe et al. result is significantly higher than the average mass fraction predicted by our model, or by the numerical simulations (i.e., according to our model $\langle f_{\text{sub}}(> 10^{-3}) \rangle = 0.145_{-0.017}^{+0.026}$). However, since the halo-to-halo variance is large, we find that the Okabe et al. measurement falls within the 95 percentile of the distribution, and can therefore be considered in agreement with Λ CDM predictions.

3.2 Formation Redshift Dependence

The upper, left-hand panel of Fig.3 plots the average subhalo mass fraction as a function of formation time, for $M_0 = 10^{11}, 10^{12}, \dots, 10^{15} h^{-1} M_{\odot}$. Earlier-forming haloes have lower

[‡] Note that the model predictions are for $f_{\text{sub}}(> 10^{-4})$; however, as is evident from the right-hand panel of Fig.2, the subhalo mass fractions $f_{\text{sub}}(> 10^{-3})$ and $f_{\text{sub}}(> 10^{-4})$ are very similar for massive host haloes.

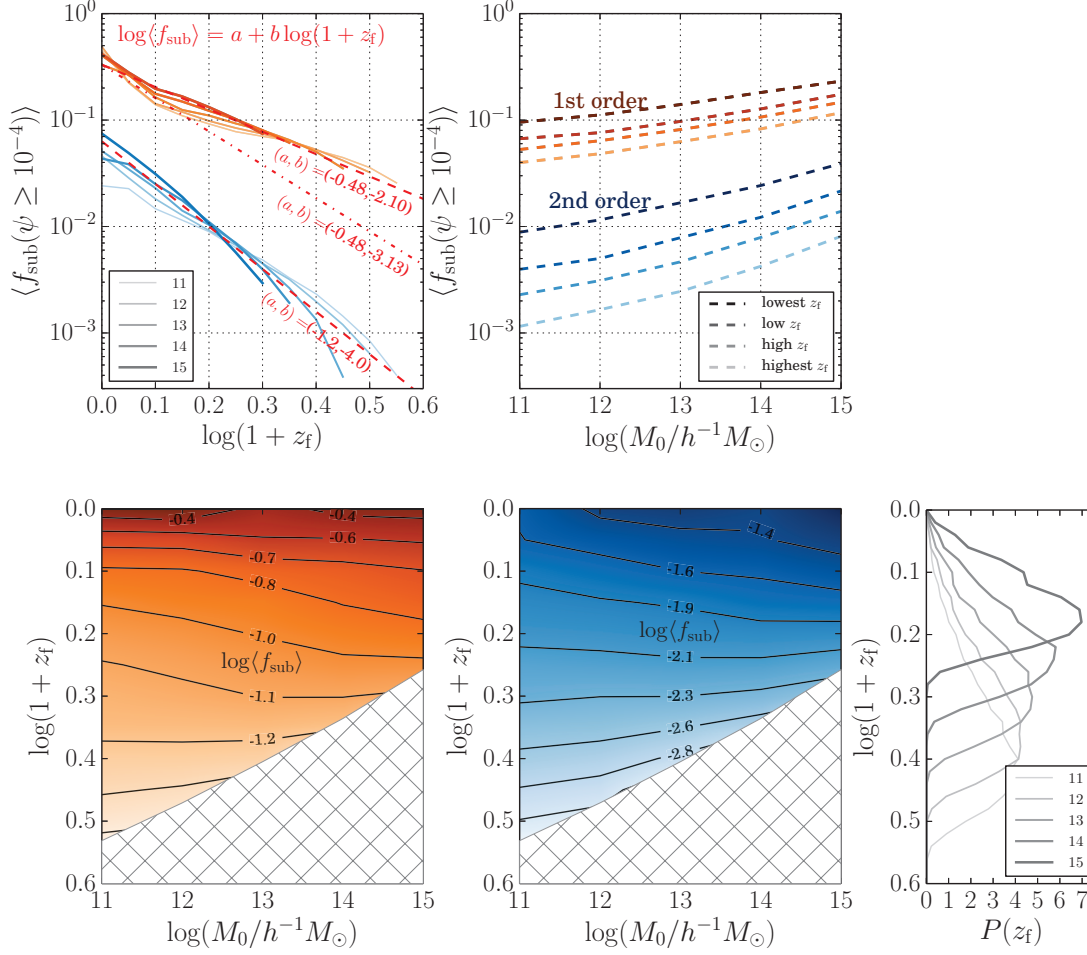


Figure 3. *Upper, left-hand panel:* the average mass fraction in subhaloes with $m > 10^{-4}M_\odot$, as a function of formation redshift, for different halo masses, as indicated. The red dashed lines are fitting functions of the form of Eq. (4) with parameters indicated in the panel. For comparison, the dash-dotted line represents the Giocoli et al. (2010) fitting function for first-order subhaloes. *Upper, right-hand panel:* $\langle f_{\text{sub}} \rangle$ as a function of M_0 for haloes of different z_f . Lines of different darkness correspond to different quartiles of the z_f -distribution, as indicated. *Lower panels:* contours of $\langle f_{\text{sub}} \rangle$ in the z_f - M_0 space of first-order (left) and second-order (right) subhaloes. *Side panel:* z_f distributions of haloes of different masses, as indicated.

subhalo mass fractions, as their subhaloes were accreted earlier and thus exposed to tidal evolution for a longer period of time (e.g., Zentner et al. 2005; van den Bosch et al. 2005; Paper I). The relation between $\langle f_{\text{sub}} \rangle$ and z_f exhibits little dependence on halo mass, and can be approximated by

$$\log \langle f_{\text{sub}} \rangle = a + b \log(1 + z_f), \quad (4)$$

with $(a, b) = (-0.48, -2.10)$ and $(-1.2, -4.0)$ for first- and second-order subhaloes, respectively.

Giocoli et al. (2010a) find a $\langle f_{\text{sub}} \rangle$ - z_f relation of the functional form of Eq.(4) but with $(a, b) = (-3.13, -0.48)$, using the GIF2 simulation. This seemingly contradicts our results: for halos with $z_f \sim 1$ the subhalo mass fraction is a factor of ~ 2 lower than our model predictions. However, their subhaloes are selected using an absolute mass cut that corresponds to $\psi \sim 10^{-2}$ for the bulk of their sample of host haloes. Since $\langle f_{\text{sub}}(\psi > 10^{-2}) \rangle$ is a factor of ~ 2 lower than $\langle f_{\text{sub}}(\psi > 10^{-4}) \rangle$, as can be seen from the right-hand panel of

Fig.2, the difference between the results of Giocoli et al. and this work simply reflects a mass-resolution effect.

The upper, right-hand panel of Fig.3 plots the average subhalo mass fraction as a function of halo mass. Different lines correspond to different quartiles in the distribution of z_f , as indicated. As is evident, the youngest quartile has a factor of ~ 2 (~ 5) more mass in first-order (second-order) subhaloes than the oldest quartile.

Finally, the lower panels of Fig.3 show contours of $\langle f_{\text{sub}} \rangle$ in the formation redshift-halo mass space. We find that, for a given z_f , $\langle f_{\text{sub}} \rangle$ is almost independent of M_0 . The hatched areas mark the regions in parameter space that contain very few haloes, as can be seen from the side-panel, which shows the z_f distributions for different halo masses. As is evident, to a good approximation $\langle f_{\text{sub}} \rangle$ is just a function of z_f , while the mass dependence simply reflects that more massive haloes assemble later (on average). We emphasize, though, that a halo's formation time does not completely determine its substructure content, as even for a fixed for-

mation time, the subhalo mass fraction reveals significant halo-to-halo variance.

3.3 Radial Profile

Dark matter subhaloes can give rise to flux-ratio anomalies in multiply imaged quasars (Dalal & Kochanek 2002; Nierenberg et al. 2014) and can cause surface brightness perturbations in the images of Einstein rings and lensed arcs (e.g., Koopmans 2005; Vegetti & Koopmans 2009; Vegetti et al. 2010, 2012, 2014; Hezaveh et al. 2016). Hence, strong gravitational lensing provides a unique window on the substructure content of dark matter haloes.

In particular, Vegetti et al. (2014) searched for subhaloes in a sample of 11 early-type lens galaxies with stellar masses of $\simeq 10^{11.5} h^{-1} M_{\odot}$ (Auger et al. 2009) at $z \simeq 0.2$ using the Sloan Lens ACS Survey (SLACS, Bolton et al. 2006). They detected subhaloes only in two systems, one with a mass $m \simeq 3.5 \times 10^9 M_{\odot}$ at an Einstein radius of $R_E \simeq 4.6$ kpc, the other with a mass $m \simeq 1.7 \times 10^{10} M_{\odot}$ at $R_E \simeq 5.05$ kpc. Combining these two detections with the non-detections, they infer a projected subhalo mass fraction of $F_{\text{sub}} = 0.0064_{-0.0042}^{+0.0080}$ (68% CL) within a median Einstein radius of $\langle R_E \rangle \simeq 4.2$ kpc.

The subhalo mass detection threshold of this SLACS sample is of the order of $10^8 h^{-1} M_{\odot}$ (Vegetti et al. 2010), while the characteristic host halo mass is $10^{13.1} h^{-1} M_{\odot}$. We obtain the latter by applying the Moster, Naab, & White (2013) stellar-to-halo mass relation (at $z = 0.2$) to the stellar masses published in Vegetti et al. (2014). Hence, a fair comparison with Λ CDM predictions requires simulations to resolve subhaloes down to $m \simeq 10^{-5} M_0$, for which it is challenging to obtain a statistically large sample of haloes. The ELVIS haloes and the cluster-size haloes in the Bolshoi simulation have sufficient resolution, but constitute a small sample of no more than 100 haloes. In addition, their masses differ from the characteristic host halo mass of the SLACS sample. On the other hand, our semi-analytical model can generate large samples of $10^{13} h^{-1} M_{\odot}$ host haloes at sufficiently high mass resolution, but provides no information regarding the radial distribution of subhaloes within their hosts. As a compromise, we use the simulations to extract information regarding the spatial distribution of subhaloes, which we apply to a statistically large sample of $10^{13.1} h^{-1} M_{\odot}$ host haloes generated with the model. This allows us to predict the halo-to-halo variance of the projected subhalo mass fraction profile, thereby allowing for a fair comparison with the lensing data.

We start by computing the radial distribution of subhaloes using the 48 Milky Way-size haloes with $M_0 = 10^{12.08 \pm 0.23}$ in the ELVIS simulation and the 38 cluster-size haloes with $M_0 > 10^{14.5} h^{-1} M_{\odot}$ in the Bolshoi simulation. In both cases we include all subhaloes with $m > 10^{-5} M_0$. The upper left-hand panel of Fig.4 plots the average number of subhaloes per unit shell volume as a function of the halo-centric distance in units of the virial radius, r/r_{vir} , and normalized to unity at r_{vir} . As is evident, the radial distribution of subhaloes in the cluster-size host haloes from the Bolshoi simulation is less concentrated than that of the Milky-Way size host haloes in ELVIS. The dashed lines correspond to the average dark matter density profiles of the corresponding host haloes, equally normalized at the virial radii. They

show that the host haloes in Bolshoi are also less concentrated on average ($\langle c_{\text{vir}} \rangle \simeq 5.6$) than those in the ELVIS simulations ($\langle c_{\text{vir}} \rangle \simeq 9.8$). The upper right-hand panel of Fig. 4 plots the average ‘radial bias’ functions, defined as the ratio between the average (normalized) subhalo distribution and the average (normalized) NFW density profile of their host haloes. Note how the Bolshoi and ELVIS results show radial bias functions that are in excellent mutual agreement. They are well fit by

$$\phi(x) \equiv \frac{d\tilde{N}/dx^3|_{\text{sub}}}{d\tilde{N}/dx^3|_{\text{NFW}}} = 2^{\mu} \frac{x^{\eta}}{(1+x)^{\mu}}, \quad x \equiv r/r_{\text{vir}} \quad (5)$$

with $(\eta, \mu) = (4.0, 2.0)$, shown as the red, dashed line. Hence, in what follows we assume that the radial bias function, $\phi(x)$, is given by this fitting function, with no dependence on halo mass [§] We also assume that the radial bias function is independent of the mass of the subhaloes. This is a valid assumption, since van den Bosch et al. (2016) have shown that there is little to no radial segregation of subhaloes by *present-day* mass.

Using the best-fit radial bias function of Eq.(5), we assign halo-centric radii to subhaloes generated by our semi-analytical model, by randomly drawing unitless halo-centric radii, $x = r/r_{\text{vir}}$ from the probability distribution $P(x) = 4\pi x^2 \phi(x) \rho(x)$, where $\rho(x)$ is the NFW density profile of the host halo in question. Next we compute the subhalo mass fraction profile as

$$f_{\text{sub}}(< x) = \left[\sum_{x_i < x} m_i \right] / M(< x | c_{\text{vir}}, M_0), \quad (6)$$

where the halo mass within radius x is given by $M(< x) = M_0 \times f(c_{\text{vir}}x)/f(c_{\text{vir}})$, with $f(x) = \ln(1+x) - x/(1+x)$.

In order to obtain a *projected* mass fraction profile, we assume that subhaloes are distributed isotropically with respect to their host centers and randomly choose a line-of-sight, so that the projected radii can be computed as $X = x \sin(\theta)$, where $\theta = \arccos(2\mathcal{R} - 1)$ with \mathcal{R} a random number drawn from a uniform distribution over $[0, 1]$. The projected subhalo mass fraction profile is computed as

$$F_{\text{sub}}(< X) = \left[\sum_{X_i < X} m_i \right] / M(< X | c_{\text{vir}}, M_0), \quad (7)$$

where the halo mass within the projected radius X is given by $M(< X) = M_0 \times g(c_{\text{vir}}x)/g(c_{\text{vir}})$, with

$$g(x) = \begin{cases} \ln\left(\frac{x}{2}\right) + \frac{1}{\sqrt{1-x^2}} \operatorname{arccosh}\left(\frac{1}{x}\right), & x < 1 \\ 1 + \ln\left(\frac{1}{2}\right), & x = 1 \\ \ln\left(\frac{x}{2}\right) + \frac{1}{\sqrt{x^2-1}} \arccos\left(\frac{1}{x}\right), & x > 1 \end{cases} \quad (8)$$

(e.g., Golse & Kneib 2002).

The solid black line in the lower left-hand panel of Fig.4 plots the median 3D subhalo mass fraction profile obtained from 2000 model realizations of haloes with $M_0 =$

[§] We note this is in conflict with Han et al. (2016), who expressed the bias function as $\phi(x) = x^{\gamma}$, and found $\gamma = 1.33$ and $\gamma = 0.95$ for Milky Way-size and cluster-size haloes, respectively. However, their results are based on a different halo finder, and on different definitions for halo mass and radius.

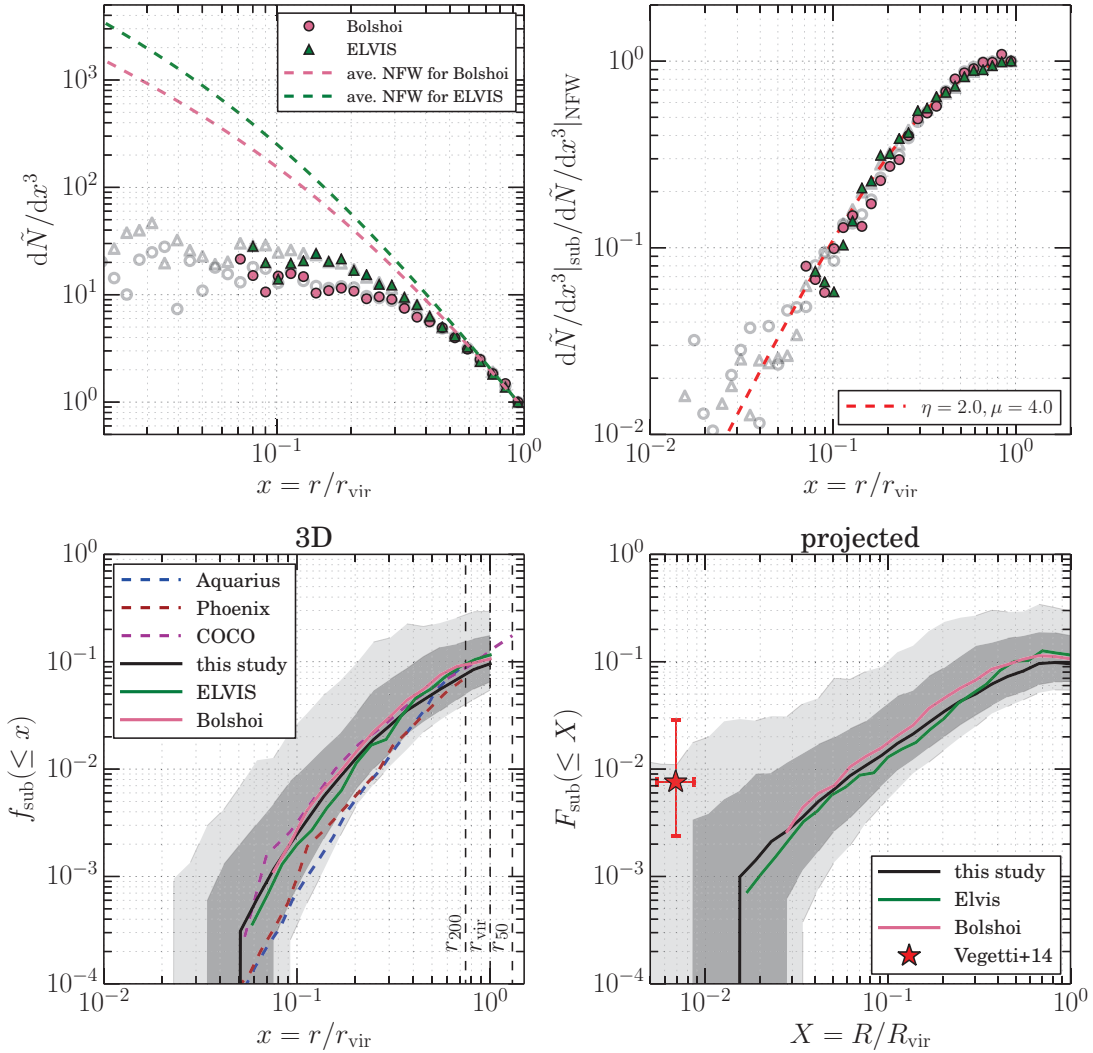


Figure 4. *Upper left-hand panel:* radial subhalo number distributions for the 48 ELVIS haloes (triangles) and the 38 Bolshoi haloes (circles) with $M_0 > 10^{14.5} h^{-1} M_\odot$, normalized at r_{vir} . Filled and open symbols indicate the median and average, respectively. The dashed lines are the average NFW profiles for the host haloes. *Upper right-hand panel:* the ‘bias function’, defined as the ratio of the normalized subhalo number distribution to the normalized density profile of the corresponding host haloes. The ‘bias’ functions for the different simulation results are indistinguishable and well fit by Eq. (5) with $\eta = 2.0$ and $\mu = 4.0$, as indicated by the red, dashed line. *Lower left-hand panel:* the median subhalo mass fraction within radius $x = r/r_{\text{vir}}$, in 3D, for different simulations (coloured lines, as indicated) and for the model (solid, black line). Note that the model prediction is obtained by drawing subhalo positions according to the universal ‘bias function’, and by assuming no radial mass segregation of subhaloes. *Lower right-hand panel:* same as lower left-hand panel, but in 2D (for a randomly chosen line-of-sight). The data point with error bars is the gravitational lensing measurement from Vegetti et al. (2014). In both lower panels the darker and lighter grey bands indicate the 68% and 90% confidence intervals around the median.

$10^{13.1} h^{-1} M_\odot$ at redshift $z_0 = 0.2$. The dark and light grey bands indicate the 68% and 95% intervals, and reflect the expected halo-to-halo variance. The other (colored) curves, correspond to simulations results, as indicated. Since these simulation results correspond to different host halo masses (Milky Way-size for ELVIS, Aquarius, and COCO, and cluster-size for Bolshoi and Phoenix), and since the subhalo mass fraction scales with halo mass (cf., Fig. 2), we rescale the simulation results to $M_0 = 10^{13.1} h^{-1} M_\odot$ using the

mass fraction-halo mass relation, $f_{\text{sub}} \propto M_0^{0.12}$. For ELVIS and Bolshoi we use the halo catalogs at $z = 0$ and $z = 0.2$, respectively, while for Aquarius, Phoenix and COCO we use the published results (corresponding to $z = 0$) from Gao et al. (2012) and Bose et al. (2016). Using the Bolshoi simulation results we have verified that there is no significant

¶ Where necessary we convert halo masses and radii to our definition of virial mass and virial radius using the concentration-mass relation of Maccio et al. (2008).

evolution in the radial bias function between $z = 0$ and $z = 0.2$, justifying the usage of $z = 0$ results. The resulting radial subhalo mass fraction profiles are overall in good mutual agreement. The Aquarius and Phoenix results are somewhat deviant, in that they give somewhat lower subhalo mass fractions at small radii. We suspect that these (small) differences arise mainly as a consequence of using different halo finders.

Finally, the lower right-hand panel of Fig.4 plots the median 2D profile for the same models, and compares them with the lensing result of Vegetti et al. (2014), represented by the data point with errorbars. The X -coordinate of the data point is obtained by dividing $\langle R_E \rangle$ by the median virial radius of the lenses, $\langle r_{\text{vir}} \rangle \simeq 427_{-87}^{+112} h^{-1} \text{kpc}$, i.e., the virial radius of a halo with $M_0 = 10^{13.1 \pm 0.3} h^{-1} M_\odot$, where we have assumed an uncertainty of 0.3dex when computing the halo mass using the Moster et al. (2013) stellar-to-halo-mass relation. As for the Okabe et al. (2014) results for Coma, the lensing measurement is much higher than the median of the model predictions or the simulation results. It does, however, fall with the 95th percentile, as indicated by the lighter grey band. Therefore we conclude that the observed subhalo mass fraction, inferred from the few gravitational lensing systems investigated so far, is noticeably higher than the median ΛCDM prediction. However, taking the large halo-to-halo variance into account, the level of disagreement does not represent a significant challenge for the ΛCDM paradigm.

We caution that our model prediction is based on dark matter only simulations. Baryonic processes can have important effects on the masses and spatial distribution of subhaloes, especially inside $\sim 1\%$ of the virial radii where the stellar mass of the central galaxy is likely to contribute significantly to the total enclosed mass. The baryonic effects on subhalo statistics is an active area of research, and there is no concordance yet regarding the extent to which baryonic physics can suppress or boost the amount of substructure (e.g., Despali & Vegetti 2016; Fiacconi et al. 2016). We will revisit this topic in a future study using a suite of high-resolution hydrodynamical zoom-in simulations.

4 HALO OCCUPATION STATISTICS

Halo occupation distributions (e.g., Berlind & Weinberg 2002; Zheng et al. 2005; Giocoli et al. 2010b) and the closely related conditional luminosity function (e.g., Yang et al. 2003; van den Bosch et al. 2013) are popular tools for modeling galaxy clustering. In such models, the primary quantity of interest is the halo occupation distribution (HOD), $P(N_{\text{gal}}|M_0)$, which expresses the probability for a halo of mass M_0 to host N_{gal} galaxies. HODs can be used, in combination with a halo mass function and a halo bias function, to predict the galaxy-galaxy two-point correlation function $\xi_{\text{gg}}(r)$, or the associated power spectrum, $P_{\text{gg}}(k)$ (e.g., Cooray & Sheth 2002; van den Bosch et al. 2013).

The HOD of galaxies is usually decomposed into a central and a satellite term: $P(N_{\text{gal}}|M_0) = P(N_{\text{cen}}|M_0) + P(N_{\text{sat}}|M_0)$. Since satellite galaxies are believed to reside in dark matter subhaloes, the satellite term is directly related to the occupation distribution of subhaloes, $P(N_{\text{sub}}|M_0)$ (Kravtsov et al. 2004). In this section we use our semi-analytical model and the simulations listed in Table 1 to

study $P(N_{\text{sub}}|M_0)$ in detail, focusing in particular on its first and second moments. In what follows we will drop the subscripts ‘sat’ and ‘sub’, and simply use N to denote the number of satellite galaxies or subhaloes (above a given mass limit).

The first moment of the HOD is given by $\langle N|M_0 \rangle = \sum_N N P(N|M_0)$, and is needed to compute the 2-halo and 1-halo central-satellite components of the power spectrum. When doing so, one implicitly makes the assumption that halo occupation statistics are completely determined by the mass of the host halo. However, this assumption is incorrect. After all, as we have shown in §3.2, for fixed M_0 the subhalo mass fraction, and hence $\langle N_{\text{sub}}|M_0 \rangle$, is strongly dependent on halo formation time. And since halo bias is also strongly dependent on halo formation time, an effect known as halo assembly bias (e.g., Gao et al. 2005, 2007; Wechsler et al. 2006), the clustering predicted with standard HOD models is systematically, and significantly, biased (e.g., Zentner et al. 2014).

To illustrate how halo formation time impacts the subhalo occupation distribution (hereafter sHOD), we use our semi-analytical model to construct 20,000 model realizations of host haloes with mass uniformly distributed over $[10^{10}, 10^{14}] h^{-1} M_\odot$. The solid, black line in Fig. 5 shows the average number of haloes with $V_{\text{max}} > 70 \text{ km s}^{-1}$, where we also count the host halo. The dashed, black line shows the corresponding number of subhaloes (i.e., the first moment of the sHOD). At each narrow bin in host halo mass, we rank-order the host haloes according to their formation redshift, z_f . The purple and cyan lines show the occupation statistics for the upper (high z_f) and lower (low z_f) quartiles, respectively. Clearly, and in line with the results from §3.2, earlier forming haloes host fewer subhaloes (see also Mao et al. 2015, who obtained very similar results using numerical simulations). Note also that the full HOD (including the host haloes) for early-forming haloes extends to smaller masses than that of its late-forming counterpart. This is simply a consequence of the fact that earlier forming haloes have higher concentrations, and therefore larger V_{max} .

The second moment of the HOD is given by $\langle N^2|M_0 \rangle = \sum_N N^2 P(N|M_0)$, and is required to compute the satellite-satellite component of the 1-halo term. The expectation value for the number of satellite-satellite pairs in a halo of mass M_0 is

$$\frac{1}{2} \langle N(N-1)|M_0 \rangle = \frac{\langle N^2|M_0 \rangle - \langle N|M_0 \rangle^2}{2}, \quad (9)$$

which allows one to compute the 1-halo satellite-satellite term of the galaxy power spectrum as

$$P_{\text{ss}}^{1\text{h}}(k) = \int_0^\infty \frac{\langle N(N-1)|M_0 \rangle}{\bar{n}^2} \tilde{u}(k|M_0)^2 n(M_0) dM_0. \quad (10)$$

Here $n(M_0)$ is the halo mass function, $\bar{n} = \int \langle N|M_0 \rangle n(M_0) dM_0$ is the average comoving number density, and $\tilde{u}(k|M_0)$ is the Fourier transform of the radial number density distribution of satellite galaxies (subhaloes).

It is common practice to assume that the number of subhaloes, and thus satellite galaxies, follows a Poisson distribution, $P(N|M_0) = \lambda^N e^{-\lambda} / N!$, with $\lambda = \langle N|M_0 \rangle$. In that case, $\langle N(N-1)|M_0 \rangle = \langle N|M_0 \rangle^2$, and therefore the

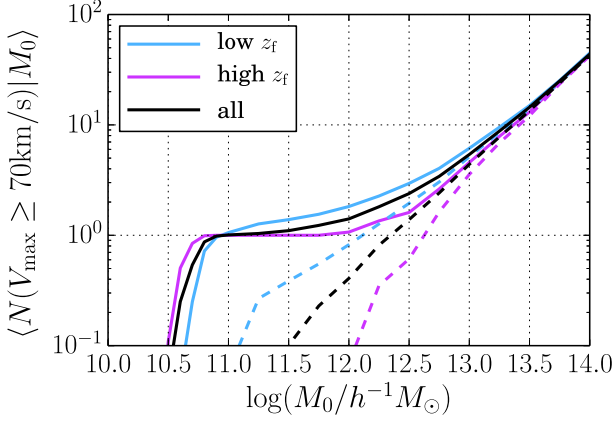


Figure 5. Illustration of assembly bias in the occupation number of subhaloes. The solid, black lines shows the first moment of the halo occupation distribution of haloes with $V_{\max} > 70 \text{ km s}^{-1}$, computed using 20,000 model realizations of haloes with mass uniformly distributed in $[10^{10}, 10^{14}] h^{-1} M_{\odot}$. The solid cyan and magenta curves show the first moments of the quartiles with the 25% youngest and oldest host haloes, respectively. Dashed lines shows the contributions due to subhaloes (i.e., satellite galaxies) only.

first moment of the HOD is sufficient to compute $P_{ss}(k)$. More generally, we may write

$$\langle N(N-1) | M_0 \rangle = \alpha^2(M_0) \langle N | M_0 \rangle^2 \quad (11)$$

where $\alpha(M_0)$ is a new function that relates the first two moments of $P(N|M_0)$. Substitution in Eq.(10) then yields

$$P_{ss}^{\text{1h}}(k) = \int_0^{\infty} \left[\alpha(M_0) \frac{\langle N | M_0 \rangle}{\bar{n}} \tilde{u}(k|M_0) \right]^2 n(M_0) dM_0. \quad (12)$$

If subhaloes (satellites) obey Poisson statistics, then $\alpha(M_0) = 1$. Similarly, if $\alpha > 1$ (< 1) we say that $P(N|M_0)$ is super- (sub-)Poissonian. As mentioned above, almost all HOD models published in the literature assume that satellite galaxies obey Poisson statistics. Notable exceptions are Cacciato et al. (2013), who instead assumed that α is independent of mass, so that it can be taken outside of the integral, and Porciani, Magliocchetti & Norberg (2004), who discussed the impact of a mass dependent α on the clustering of quasars.

But how accurate is the assumption of a Poissonian $P(N|M_0)$? Semi-analytic models and hydrodynamic simulations predict a $P(N_{\text{gal}}|M_0)$ that is significantly sub-Poissonian whenever $\langle N_{\text{gal}}|M_0 \rangle$ is small (e.g., Benson et al. 2000; Seljak 2000; Berlind et al. 2003). In fact, it was realized early on that in order for HOD models to produce galaxy-galaxy correlation functions with a power-law-like form as observed, $P(N_{\text{gal}}|M_0)$ indeed needs to be sub-Poissonian (e.g., Benson et al. 2000; Seljak 2000; Scoccamarro et al. 2001; Berlind & Weinberg 2002). However, this does not necessarily imply that $P(N_{\text{sat}}|M_0)$ has to be sub-Poissonian as well. In fact, if $P(N_{\text{sat}}|M_0)$ is Poissonian, then as long as $\langle N_{\text{sat}}|M_0 \rangle = \langle N_{\text{gal}}|M_0 \rangle - 1$ (which holds as long as M_0 is large enough so that the halo always hosts a central galaxy), one has that

$$\frac{\langle N_{\text{gal}}(N_{\text{gal}} - 1) | M_0 \rangle}{\langle N_{\text{gal}} | M_0 \rangle^2} = 1 - \frac{1}{\langle N_{\text{gal}} | M_0 \rangle^2} \quad (13)$$

(Kravtsov et al. 2004). Hence, $P(N_{\text{gal}}|M_0)$ will be sub-Poissonian unless $\langle N_{\text{gal}}|M_0 \rangle$ is large. Using numerical simulations, Kravtsov et al. (2004) argued that the occupation distribution of *subhaloes*, $P(N_{\text{sub}}|M_0)$, is well described by a Poisson distribution (in that $\alpha \sim 1$), although they did find evidence for sub-Poissonian behavior at small $\langle N_{\text{sub}}|M_0 \rangle$. More recently, Boylan-Kolchin et al. (2010, hereafter BK10) pointed out that the sHOD is actually strongly super-Poissonian when $\langle N|M_0 \rangle$ is large, even though $\alpha \sim 1$ (see also Busha et al. 2011; Wu et al. 2013). This can come about because one can rewrite Eq. (11) as

$$\alpha^2(M_0) = 1 + \frac{1}{\langle N | M_0 \rangle} \left(\frac{\sigma^2(M_0)}{\sigma_P^2(M_0)} - 1 \right) \quad (14)$$

Here $\sigma^2(M_0)$ is the variance of $P(N|M_0)$ and $\sigma_P^2(M_0)$ is the variance of a Poissonian $P(N|M_0)$ with the same mean. Hence, when $\langle N|M_0 \rangle$ is large, even a strongly non-Poissonian distribution will have a value for α close to unity. Mao et al. (2015) argue that the super-Poissonian character of the sHOD arises from variance in the large-scale environments of the host haloes, and that the sHOD is actually Poissonian for host haloes in a fixed large-scale environment.

In the following subsections, we characterize in detail how the sHOD deviates from a Poisson distribution. We show that it is both sub-Poissonian at small $\langle N|M_0 \rangle$ and super-Poissonian at large $\langle N|M_0 \rangle$, and present an accurate fitting function for $\alpha(\langle N \rangle)$ (§4.2). Next we discuss the implications of the non-Poissonity for galaxy clustering (§4.3), and how the detailed shape of the sHOD depends on how subhaloes are selected (§4.4). Finally, in §4.5 we show that, contrary to the claim by Mao et al. (2015), non-Poissonity cannot be eliminated by selecting haloes of fixed formation time. However, we first test to what accuracy our semi-analytical model can reproduce the detailed shape of the sHOD as inferred from numerical simulation.

4.1 Model versus Simulations

The semi-analytical model has proven to be accurate in predicting the average subhalo mass and velocity functions (Paper I & II), as well as the halo-to-halo variance of the v_{\max} distributions of massive subhaloes (Jiang & van den Bosch et al. 2015). Here we further examine the accuracy of the model, focusing on the halo-to-halo variance in subhalo number, $\langle N(\geq \psi) \rangle$, over a wide range of subhalo mass, $\psi = m/M_0$.

We consider 10,000 model realizations of haloes with $M_0 = 10^{13.75 \pm 0.25} h^{-1} M_{\odot}$, and the 1231 Bolshoi haloes in the same mass range. The left-hand panel of Fig.6 compares $\langle N(\geq \psi) \rangle$ of the model realizations, to that of the Bolshoi haloes. The model is generally in good agreement with the simulation in terms of the average, as well as the halo-to-halo variance at the massive end, but it underestimates the scatter at the low-mass end. This is better revealed in the right-hand panels of Fig.6, which compare the model and Bolshoi sHODs, for three different mass thresholds at which $\langle N(\geq \psi) \rangle = 2, 8, \text{ and } 20$ respectively. For $\langle N \rangle = 2$ the Bolshoi simulation results reveal a clear departure from a Poisson distribution, which is accurately reproduced by the model. Hence, the semi-analytical model seems to reproduce the sub-Poissonian behavior of the sHOD for small $\langle N \rangle$.

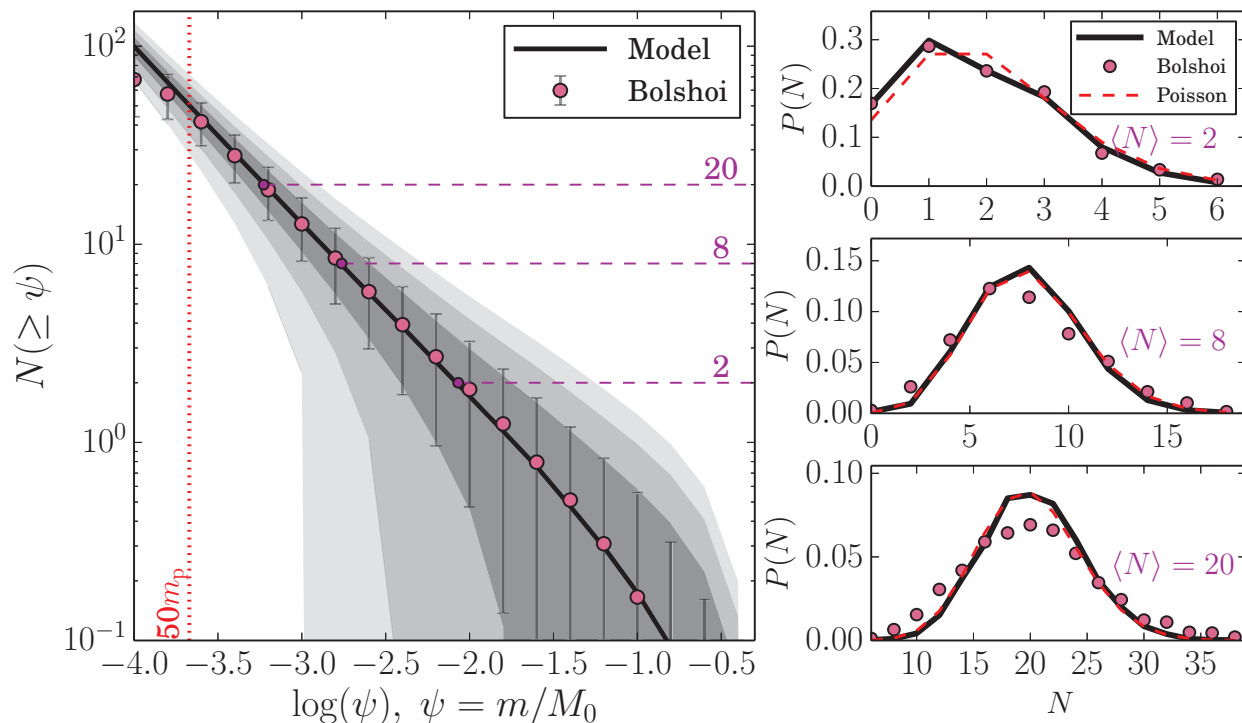


Figure 6. Subhalo Occupation Statistics. *Left-hand panel:* the average, cumulative subhalo mass function, $\langle N(\geq \psi) \rangle$, for 10,000 model realizations of haloes with $M_0 = 10^{13.75 \pm 0.25} h^{-1} M_\odot$ (solid, black line), compared with that of the 1231 Bolshoi haloes in the same mass range (symbols). The progressively lighter grey bands indicate the $\pm 1, 2$, and 3σ scatter around the average, while the errorbars indicate the $\pm 1\sigma$ scatter in Bolshoi, where $\sigma = \sqrt{\text{Var}(N)}$. The vertical dotted line indicates the Bolshoi resolution limit of $50m_p$. *Right-hand panels:* subhalo occupation distributions, $P(N(\geq \psi)|M_0)$, for different mass thresholds, ψ , for which $\langle N \rangle = 2, 8$, and 20 (as indicated). The model prediction (solid line) starts to disagree with the Bolshoi results (symbols) as $\langle N \rangle$ increases. The red, dashed curves correspond to Poisson distributions with the same $\langle N \rangle$, and are shown for comparison. See text for a detailed discussion.

However, when $\langle N \rangle$ becomes large, the sHOD from the Bolshoi simulation becomes super-Poissonian, something that is *not* captured by the semi-analytical model, which instead predicts sHODs that are perfectly Poissonian.

This failure of the semi-analytical model to reproduce the strongly super-Poissonian nature of the sHOD, is most likely due to the fact that the halo merger trees in the model are generated using the Parkinson et al. (2008) algorithm, which is based on the extended Press-Schechter (EPS) theory. EPS describes the assembly of dark matter haloes using Markovian excursion sets, which means that halo mass increments are assumed to be uncorrelated. As shown by Neistein & Dekel (2008), this is not representative of how haloes assemble in numerical simulations, and explains why the standard (i.e., Markovian) EPS formalism fails to capture the non-Poissonity of subhalo statistics *accretion*. We conclude that despite the model’s successes, it is not suitable for predicting the detailed shape of the sHOD (at least not for $\langle N \rangle \gtrsim 2$). Hence, in what follows we primarily use the Bolshoi and MultiDark simulations to study the non-Poissonity of $P(N|M_0)$.

4.2 Non-Poissonity

The upper panel of Fig.7 plots the standard deviation of the subhalo number counts, $\sigma = \sqrt{\text{Var}(N)}$, in units of that of a Poisson distribution, $\sigma_P = \sqrt{\langle N \rangle}$, as a function of the average subhalo number, $\langle N \rangle$. Here we use the 1231 Bolshoi haloes with $M_0 = 10^{13.75 \pm 0.25} h^{-1} M_\odot$ and the 2393 MultiDark haloes with $M_0 = 10^{14.75 \pm 0.25} h^{-1} M_\odot$. The Bolshoi and MultiDark results are plotted up to $\langle N(\geq \psi_{\text{res}}) \rangle$, where $\psi_{\text{res}} = M_{\text{res}}/M_0 \simeq 10^{-3.7}$ and $10^{-2.9}$ respectively, with M_{res} the mass of 50 particles. The halo mass scales are chosen as a compromise between sample size and dynamical range: more massive haloes are better resolved than lower-mass haloes, thereby allowing one to probe the behavior to larger $\langle N \rangle$. On the other hand, one needs of the order of 1000 haloes to reliably probe the statistics at small $\langle N \rangle$, and the number density of massive haloes is limited. We have verified, though, using haloes of different mass scales in Bolshoi and MultiDark, that the results exhibit little dependence on halo mass. Also plotted, for comparison, are the published results for the 96 haloes in the ‘Rhapsody-4K’ simulation with $M_0 = 10^{14.8 \pm 0.05} h^{-1} M_\odot$ (Wu et al. 2013). Taken together, these simulation results reveal that the scatter in $P(N_{\text{sub}}|M_0)$ is super-Poissonian ($\sigma/\sigma_P > 1$) when $\langle N \rangle$ is

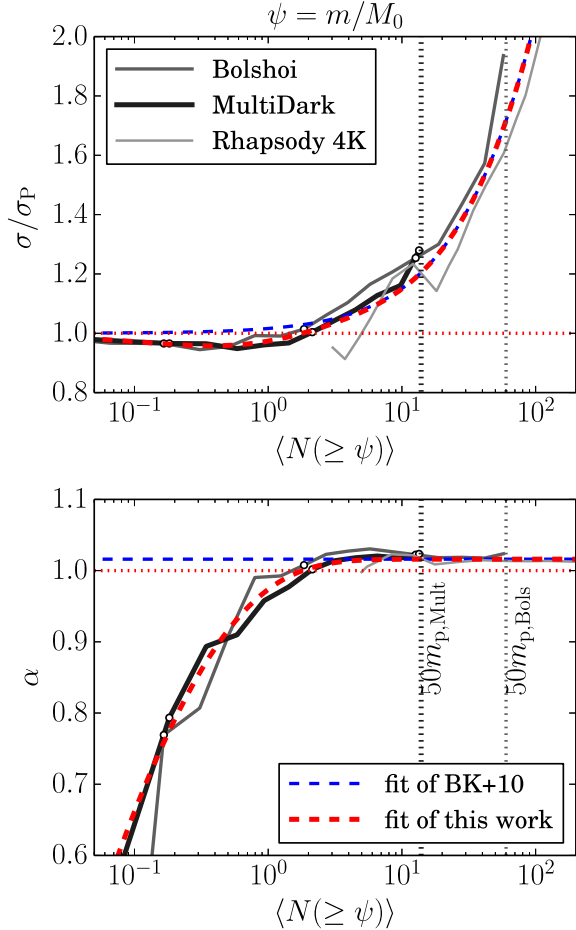


Figure 7. *Upper panel:* halo-to-halo variance of subhalo number, $\sigma = \sqrt{\text{Var}(N)}$, in units of the corresponding Poisson scatter, $\sigma_P = \sqrt{\langle N \rangle}$, as a function of the average cumulative number of subhaloes, $\langle N(\geq \psi) \rangle$. Shown in solid lines are the Bolshoi result for the 1231 haloes with $M_0 = 10^{13.75 \pm 0.25} h^{-1} M_\odot$, the 2393 MultiDark result for haloes with $M_0 = 10^{14.75 \pm 0.25} h^{-1} M_\odot$, and the 96 Rhapsody haloes with $M_0 = 10^{14.8 \pm 0.05} h^{-1} M_\odot$, as indicated. The cyan, dashed line indicates the model of BK10 based on the MS-II simulation (Eq. [15]), while the red dashed line is the new fitting function proposed here (Eq. [16]). Vertical, dotted lines indicate the 50-particle resolution limits of the Bolshoi and MultiDark simulations, as indicated. *Lower panel:* Same as the upper panel, but for $\alpha \equiv \langle N(N-1) \rangle^{1/2} / \langle N \rangle$, which is the parameter relevant for HOD modeling of galaxy clustering.

large, and sub-Poissonian ($\sigma/\sigma_P < 1$) when $\langle N \rangle$ is small, with the transition occurring at $\langle N \rangle \sim 2$.

The sub-Poissonian scatter at small $\langle N \rangle$ is better revealed in the lower panel of Fig.7, which plots the α -statistic (Eq. [14]) as a function of $\langle N \rangle$. At large $\langle N \rangle$, α in different simulations converge to a constant that is slightly larger than unity, while at small $\langle N \rangle$, α drops below unity.

The super-Poissonian behavior at large- $\langle N \rangle$ is well known. Based on the results from the Millennium-II simulation (hereafter MS-II), BK10 describe the halo-to-halo variance as the sum of two terms, $\sigma^2 = \sigma_P^2 + \sigma_I^2$. The first term is the Poissonian scatter, $\sigma_P^2 = \langle N \rangle$; while the second term reflects *intrinsic* scatter. Fitting to the MS-II results,

they find that, to good approximation, $\sigma_I^2 = (0.18\langle N \rangle)^2$. Therefore, σ/σ_P can be expressed as

$$\frac{\sigma}{\sigma_P} = \sqrt{1 + \epsilon^2 \langle N \rangle}, \quad (15)$$

with $\epsilon = 0.18$. As shown in Fig.7 (blue dashed curve), this simple, empirical model also nicely fits the Bolshoi and MultiDark results at $\langle N \rangle \gg 2$. However, it does not capture the sub-Poissonian scatter at $\langle N \rangle \lesssim 2$: according to Eqs.(15) and (14), the BK10 model yields $\alpha = \sqrt{1 + \epsilon^2} = 1.016$, independent of $\langle N \rangle$. We emphasize that our results are not inconsistent with the MS-II simulation. Rather, the latter simply lacks sufficient statistical power to probe the behavior of σ/σ_P at small $\langle N \rangle$. In fact, Fig. 8 in BK10 already hints at sub-Poissonian behavior at small $\langle N \rangle$, at least for the more massive host haloes, at low significance.

We find that the sub-Poissonian scatter can be taken into account by multiplying the expression for σ/σ_P of Eq.(15) with a ‘correction factor’ according to

$$\frac{\sigma}{\sigma_P} = (1 - \eta x^2 e^{-x}) \sqrt{1 + \epsilon^2 \langle N \rangle}, \quad (16)$$

where $x = \sqrt{\langle N \rangle / N_0}$, with $\eta = 0.09$, $N_0 = 0.12$, and $\epsilon = 0.18$. As is evident from Fig.7 (red dashed curve), this model accurately describes the simulation results over the entire range of $\langle N \rangle$ covered. In particular, for $\langle N \rangle \gg 1$, it reduces to Eq.(15), such that the asymptotic value of α is still $\sqrt{1 + \epsilon^2}$, in agreement with BK10.

4.3 Implications for Satellite Clustering

Since α is a function of $\langle N \rangle$, and $\langle N \rangle$ depends on halo mass M_0 , we have that $\alpha = \alpha(M_0)$. Here we illustrate the influence of a mass-dependent α on the galaxy power spectrum. In particular, we show how the non-Poissonity as described by Eq. (16) impacts the galaxy power spectrum $P_{\text{gg}}(k)$, but comparing with the case were $\alpha = 1$, as is commonly assumed.

Splitting the galaxy population in centrals and satellites, and ignoring (for simplicity) shot-noise, we can write the galaxy power spectrum as

$$P_{\text{gg}}(k) = 2P_{\text{cs}}^{1\text{h}}(k) + P_{\text{ss}}^{1\text{h}}(k) + P_{\text{cc}}^{2\text{h}}(k) + 2P_{\text{cs}}^{2\text{h}}(k) + P_{\text{ss}}^{2\text{h}}(k), \quad (17)$$

(e.g., van den Bosch et al. 2013). Here the super-scripts ‘1h’ and ‘2h’ refer to the one- and two-halo term, respectively, while ‘c’ and ‘s’ refer to centrals and satellites.

Following van den Bosch et al. (2013), and ignoring halo exclusion and scale dependence of the halo bias, we have that

$$P_{\text{cs}}^{1\text{h}}(k) = \int_0^\infty \mathcal{H}_c(k, M_0) \mathcal{H}_s(k, M_0) n(M_0) dM_0. \quad (18)$$

$$P_{\text{ss}}^{1\text{h}}(k) = \int_0^\infty \alpha^2(M_0) \mathcal{H}_s^2(k, M_0) n(M_0) dM_0. \quad (19)$$

and

$$P_{\text{xy}}^{2\text{h}}(k) = P_{\text{in}}(k) \int_0^\infty \mathcal{H}_x(k, M_0) n(M_0) b_{\text{h}}(M_0) dM_0 \int_0^\infty \mathcal{H}_y(k, M_0) n(M_0) b_{\text{h}}(M_0) dM_0. \quad (20)$$

Here, x and y are either c (for central) or s (for satellite),

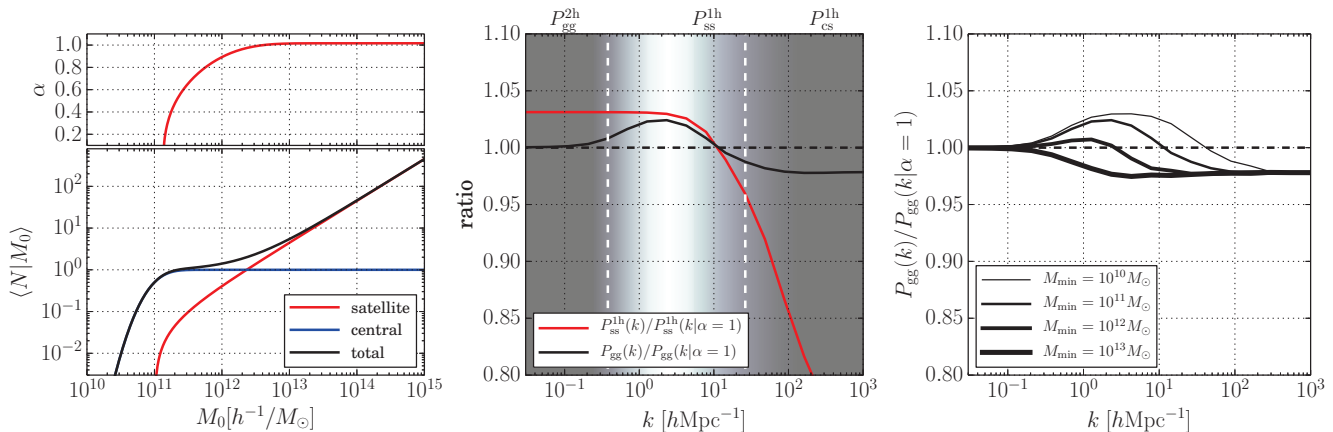


Figure 8. Illustration of the impact of non-Poissonian subhalo statistics on the galaxy power spectrum. *Left-hand panel:* The lower panel shows the first moment of the occupation statistics of satellites (red), centrals (blue), and all galaxies (black) for our HOD with $M_{\min} = 10^{11} h^{-1} M_{\odot}$, which roughly corresponds to $V_{\max} = 70 \text{ km s}^{-1}$. The upper panel plots the corresponding α , computed using our fitting function as described in the text. *Middle panel:* the ratio of the galaxy power spectrum computed using the $\alpha(M_0)$ relation given in the upper left-hand panel, to that computed using $\alpha = 1$ (as is commonly done). Red and black curves correspond to the one-halo satellite-satellite term, $P_{\text{ss}}^{1h}(k)$, and the full power spectrum, $P_{\text{gg}}(k)$, respectively, while the grey scale reflects the fractional contribution of P_{ss}^{1h} to the total power P_{gg} (lighter grey tones indicating a larger contribution). The vertical lines bracket the regime where P_{ss}^{1h} contributes more than 50% of the total power. *Right-hand panel:* Same as the solid curve in the middle panel, but for different values of M_{\min} , as indicated. Note how ignoring the non-Poissonity introduces systematic errors of up to ~ 3 percent, and with a complicated scale- and M_{\min} -dependence.

$n(M_0)$ is the halo mass function, $b_h(M_0)$ is the linear halo bias function, and we have used the shorthand notation

$$\mathcal{H}_c(k, M_0) = \frac{\langle N_{\text{cen}} | M_0 \rangle}{\bar{n}} \quad (21)$$

and

$$\mathcal{H}_s(k, M_0) = \frac{\langle N_{\text{sat}} | M_0 \rangle}{\bar{n}} \tilde{u}(k | M_0) \quad (22)$$

with \bar{n} the total number density of all galaxies (centrals plus satellites), and $\tilde{u}(k | M_0)$ the Fourier transform of the radial number density distribution of satellite galaxies in a halo of mass M_0 . Note that centrals are assumed to reside at rest at the center of their host halo.

In what follows, we adopt the halo mass and halo bias functions of Tinker et al. (2008, 2010) for haloes that are defined to have an overdensity with respect to the average matter density of $\Delta_m = 360^{\parallel}$. In addition, we assume that satellites follow a radial number density distribution given by an NFW profile with the concentration-mass relation of Neto et al. (2007). The corresponding expression for $\tilde{u}(k | M_0)$ is given in Scoccimarro et al. (2001). Finally, we adopt the following HOD model for the centrals and satellites:

$$\langle N_{\text{cen}} | M_0 \rangle = \frac{1}{2} [1 + \text{erf}[(\log M_0 - \log M_{\min})/0.3]] \quad (23)$$

and

$$\langle N_{\text{sat}} | M_0 \rangle = \begin{cases} 0.045 \left(\frac{M_0}{M_{\min}} - 1 \right), & M_0 > M_{\min} \\ 0, & M_0 < M_{\min} \end{cases} \quad (24)$$

with $M_{\min} = 10^{11} h^{-1} M_{\odot}$. There is no particular reason for

picking this HOD model other than that it is representative of typical HOD models used in the literature. The second moment of the satellite occupation statistics is characterized by $\alpha(M_0)$, which is given by the combination of Eqs. (14), (16), and (24).

The left-hand panels of Fig.8 plot $\langle N | M_0 \rangle$ and $\alpha(M_0)$ corresponding to this HOD model. The red, solid curve in the middle panel of Fig.8 plots the ratio between $P_{\text{ss}}^{1h}(k)$ and $P_{\text{ss}}^{1h}(k | \alpha = 1)$. Note how the M_0 -dependence of α reduces the clustering power at small scales (large- k) while enhancing it (by about 3 percent) on large scales (small- k). The grey-scale reflects the fractional contribution of this satellite-satellite 1-halo term to the total power spectrum, $P_{\text{gg}}(k)$, with a darker grey-tone reflecting a small contribution: on large scales the 2-halo term dominates, while the central-satellite 1-halo term dominates on small scales. The black, solid curve in the middle panel of Fig.8 plots the ratio between $P_{\text{gg}}(k)$ and $P_{\text{gg}}(k | \alpha = 1)$, which is basically unity on large scales (small- k). However, for $k \gtrsim 1 h \text{Mpc}^{-1}$ ignoring the non-Poissonity of the sHOD can result in systematic errors in the galaxy power-spectrum of up to ~ 3 percent. In particular, it will underpredict the power by ~ 3 percent on intermediate scales ($k \sim 3 h \text{Mpc}^{-1}$), and overpredict the power by ~ 2 percent on very small scales ($k > 100 h \text{Mpc}^{-1}$). Finally, the right-hand panel of Fig.8 plots $P_{\text{gg}}(k)/P_{\text{gg}}(k | \alpha = 1)$ for four different values of M_{\min} , as indicated. Roughly speaking, lower values of M_{\min} corresponds to HODs of fainter galaxies. As is evident, the non-Poissonity of the sHOD manifests itself differently for different luminosity-threshold samples of galaxies; typically, the power spectra of fainter galaxies are more susceptible to the detailed shape of the sHOD (i.e., show a larger deviation from the case with $\alpha = 1$). Hence, simply making the naive assumption that the occupation statistics of satellite

^{||} Using interpolation of the mass and bias functions presented in Tinker et al. for different values of Δ_m .

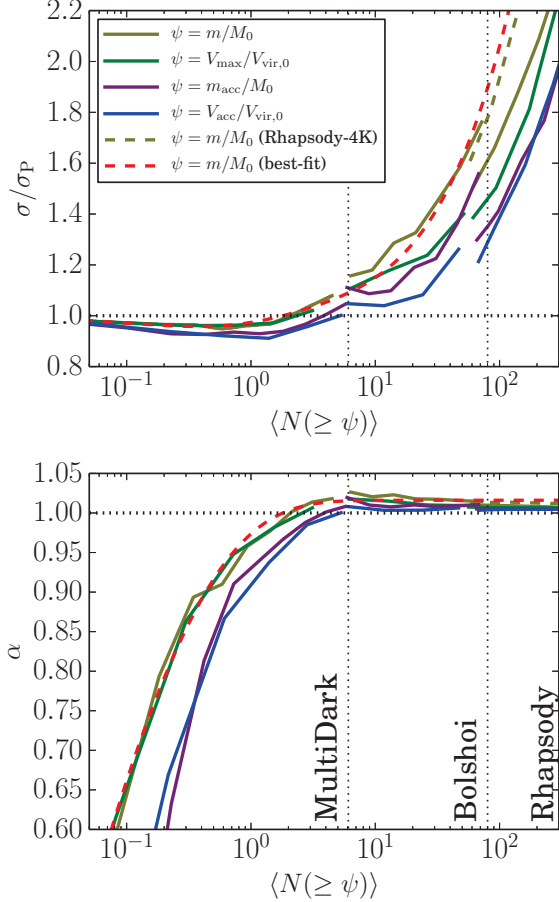


Figure 9. Dependence of non-Poissonity on subhalo selection. The upper and lower panels plot, respectively, σ/σ_P and α as functions of $\langle N(\geq \psi) \rangle$, for $\psi = m/M_0$, $v_{\max}/V_{\text{vir},0}$, m_{acc}/M_0 , and $v_{\text{acc}}/V_{\text{vir},0}$. From small- $\langle N \rangle$ to large- $\langle N \rangle$, we use the results for MultiDark haloes with $M_0 = 10^{14.75 \pm 0.25} h^{-1} M_\odot$, Bolshoi haloes with $M_0 = 10^{14.25 \pm 0.25} h^{-1} M_\odot$, and Rhapsody haloes with $M_0 = 10^{14.8 \pm 0.05} h^{-1} M_\odot$, respectively. The two vertical dotted lines indicate the mass scales where subhaloes have 100-particles in the MultiDark and Bolshoi simulation, as indicated. The red, dashed lines correspond to the same fitting function as shown in Fig.7, which best describes the m -selected samples. Using a selection based on m_{acc} or v_{acc} yields weaker super-Poissonity at high- $\langle N \rangle$ and stronger sub-Poissonity at low- $\langle N \rangle$, compared to the selection based on m or v_{\max} . The dashed, ochre line is result based on m -selection for the Rhapsody-4K simulation. It reveals stronger super-Poissonity than for the higher-resolution, fiducial Rhapsody-8K simulation, suggesting that the simulation results have not yet fully converged.

galaxies are Poissonian results in systematic errors in the galaxy-power spectrum (and thus also in the corresponding two-point correlation function) at the level of a few percent, and with a complicated scale- and luminosity-dependence. Although small, such errors are funest for any attempt to use galaxy clustering to do precision (i.e. percent-level) cosmology.

4.4 Dependence on Subhalo Selection

Wu et al. (2013) found that selecting subhaloes by their *present-day* mass or v_{\max} results in stronger super-Poissonity than selecting by their mass or v_{\max} *at accretion*. Their result is based on the relatively small sample of 96 Rhapsody haloes and limited to the regime where $\langle N \rangle \gtrsim 100$. We now revisit this issue using much larger samples from the Bolshoi and MultiDark simulations, with the goal to characterize in detail how $\alpha(\langle N \rangle)$ depends on how subhaloes are selected.

Fig.9 plots σ/σ_P and α as functions of $\langle N(\geq \psi) \rangle$ for different choices of ψ . The MultiDark, Bolshoi, and Rhapsody results are plotted for small-, intermediate-, and large- $\langle N \rangle$, respectively. The red, dashed lines represent the same fitting functions as shown in Fig.7, which accurately describe the results for $\psi = m/M_0$ and serve as reference lines to facilitate the comparison. A few trends are evident. First, confirming the Wu et al. (2013) result, we find weaker super-Poissonity for m_{acc} - and v_{acc} -selected subhaloes. However, at small $\langle N \rangle$, m_{acc} - or v_{acc} -selection results in a stronger sub-Poissonity compared to a selection based on m or v_{\max} . The m_{acc} - and v_{acc} -selected samples behave extremely similar; both have a σ/σ_P - $\langle N \rangle$ dependence that is well approximated by Eq.(16) with $\eta = 0.16$, $N_0 = 0.2$, and $\epsilon = 0.1$. Second, whereas the results for MultiDark and Bolshoi nicely agree around their transition at $\langle N \rangle = 5$, this is not the case for Bolshoi and Rhapsody, which reveal a pronounced ‘jump’ in σ/σ_P around their transition at $\langle N \rangle = 80$, especially for m and m_{acc} . Interestingly, though, the result from the lower-resolution Rhapsody-4K, shown as the dashed, green-yellow line for $\psi = m/M_0$ only, matches the Bolshoi results extremely well. This suggests that the super-Poissonity at large- $\langle N \rangle$ may be sensitive to resolution effects in the numerical simulation. Hence, we caution that the model for $\alpha(\langle N \rangle)$ presented in §4.2 is only as good as the simulations used, and may be impacted by numerical resolution effects.

4.5 Environmental Effects

Mao et al. (2015) suggest that the non-Poissonity of the sHOD originates from the large-scale environment of the host haloes. In particular, they argue that host haloes of the same mass and with the same large scale environment have a Poissonian sHOD, and that the super-Poissonity is a consequence of ‘convolving’ this Poissonian sHOD with a distribution of environments, each having a slightly different, albeit Poissonian, sHOD. Based on this notion, they devise a simple model for the subhalo v_{\max} function, in which the *average* subhalo abundance, $\langle N(\geq v_{\max}) \rangle$, is a function of the ratio $V_{\max}/V_{\text{vir},0}$ of the host halo. In addition, for a given $V_{\max}/V_{\text{vir},0}$ it is assumed that $N(\geq v_{\max})$ follows Poisson statistics. Hence, Mao et al. (2015) treat $V_{\max}/V_{\text{vir},0}$ as their environment proxy, which is motivated by the fact that $V_{\max}/V_{\text{vir},0}$ depends on halo concentration, which depends on the halo formation time, z_f , which in turn depends on the halo’s large scale environment (e.g., Wechsler et al. 2002; Hearin, Behroozi & van den Bosch 2016).

In order to test this claim by Mao et al. (2015), we investigate whether the non-Poissonity of the sHOD diminishes if we select host haloes based on both mass and formation redshift z_f ; i.e., we treat halo formation time as a proxy

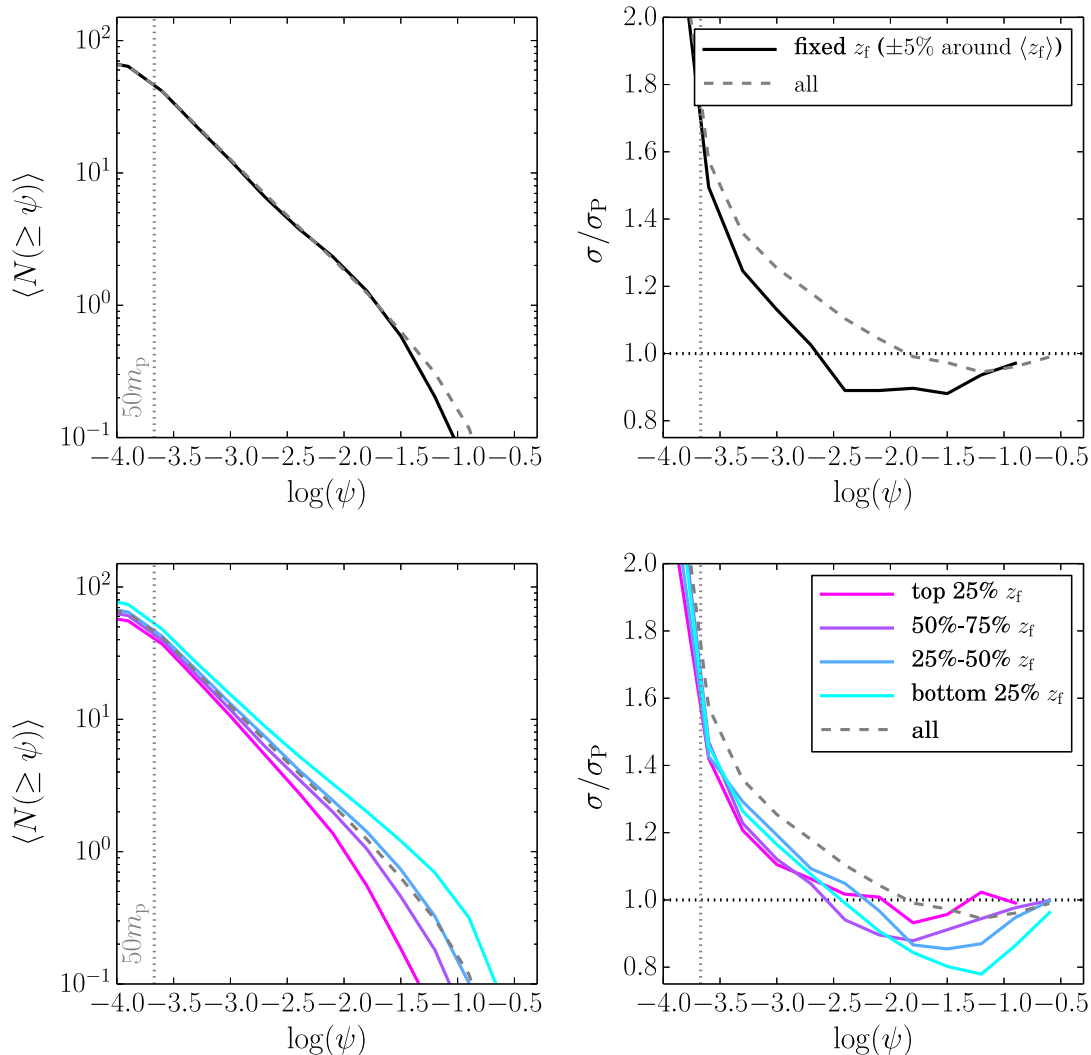


Figure 10. *Upper left-hand panel:* The grey, dashed curve shows the average, cumulative mass function, $\langle N(\geq \psi) \rangle$, for all haloes in the Bolshoi simulation with $M_0 = 10^{13.75 \pm 0.25} h^{-1} M_\odot$. The solid, black line corresponds to the subset of host haloes that have formation redshifts in a narrow ($\pm 5\%$ percentile) range centered around the median z_f . *Upper right-hand panel:* the corresponding ratios σ/σ_P . Note how restricting z_f to a narrow range the super-Poissonity becomes weaker while the sub-Poissonity becomes stronger. *Lower panels:* same as upper panels, but this time showing results for the four different quartiles in formation redshift, as indicated. Note how older host haloes have subhalo occupation statistics that are closer to Poissonian.

for a host halo’s large scale environment. As a first test, we select a subsample of the 1231 Bolshoi host haloes with $M_0 = 10^{13.75 \pm 0.25} h^{-1} M_\odot$ that have a formation redshift, z_f , in the very narrow range, $z_f = 0.71 \pm 0.3$. This corresponds to the ± 5 percentile range centered around the median formation redshift. The upper left-hand panel of Fig.10 plots the average, cumulative subhalo mass functions, $\langle N(\geq \psi) \rangle$, for all subhaloes in the mass bin, and for those in the ± 5 percentile range centered on the median z_f . As expected, choosing haloes with z_f around the median z_f has little impact on the average subhalo mass function. However, as is evident from the upper right-hand panel, the variance of the ‘fixed- z_f ’ subsample is fairly different from that of the full sample. In particular, the super-Poissonity at the low-mass end is weaker, while the sub-Poissonity at the massive

end is enhanced. Put differently, the transition from super-Poissonian to sub-Poissonian shifts from $\psi = m/M_0 \simeq 0.016$ to $m/M_0 \simeq 0.002$ (or equivalently from $\langle N \rangle \simeq 2$ to $\langle N \rangle \simeq 5$). Although not shown here, we have verified that qualitatively similar behavior is observed if we adopt halo concentration as the environment proxy and select a subsample of haloes with fixed c_{vir} .

In order to portray more clearly how σ/σ_P depends on formation time, we bin the Bolshoi haloes with $M_0 = 10^{13.75 \pm 0.25} h^{-1} M_\odot$ into z_f quartiles and plot their average subhalo mass functions $\langle N(\geq \psi) \rangle$ and variance ratio σ/σ_P in the lower panels of Fig.10. As is evident from the lower left-hand panel, and as discussed in detail in §3.2, older haloes (i.e., those with higher z_f) contain more subhaloes than younger haloes of the same mass. The difference is most

pronounced at the massive end, consistent with the results of Gao et al. (2011) based on the MS-II simulation. In terms of the σ/σ_P , there is a clear trend that the sHOD of younger host haloes deviates more strongly from a Poisson distribution. Since older haloes acquire their subhaloes earlier and tend to be more dynamically relaxed, this suggests that the dynamical evolution of subhaloes (mass stripping and tidal disruption) drives the sHOD towards a Poisson distribution.

To summarize, we agree with Mao et al. (2015) that the detailed shape of the sHOD depends on the large scale environment of the host haloes, at least in as far as this environment is correlated with halo formation time. The main trend is for the sHOD to become more Poissonian with increasing halo formation time. However, we see no indication to support their claim that the sHOD is Poissonian for a fixed environment. Consequently, their model for $\langle N(\geq v_{\max}) \rangle$ is likely to be oversimplified. Mao et al. (2015) based their conclusion on a suite of 13 zoom-in simulations of a Milky Way-size halo. Each simulation has the same large scale modes (representative of the large scale environment), but differ in the initial phases of the small-scale modes with $k \gtrsim 16.4h/\text{Mpc}$ (comoving). They find that the subhaloes in this suite obey Poisson statistics (i.e., $\sigma/\sigma_P \simeq 1$) when $\langle N(\geq \psi) \rangle$ is large. However, the Lagrangian volume within which the initial conditions are randomized is very small compared to that of entire host halo: $k = 16.4h/\text{Mpc}$ corresponds to a scale of $\lambda \simeq 2\pi/k \simeq 0.38 h^{-1}\text{Mpc}$, while a Milky Way-size halo ($M_0 \sim 10^{12} h^{-1}M_\odot$) corresponds to a Lagrangian volume of radius $r_L = [3M_0/(4\pi\rho_m)]^{1/3} \sim 1.44 h^{-1}\text{Mpc}$, which is more than three times larger than λ . In other words, the mass fraction of the host halo for which Mao et al. randomize the modes is only $(\lambda/r_L)^3 \simeq 0.019$. Consequently, these 13 zoom-in simulations have virtually identical mass accretion histories, only differing in their accretion of low mass subhaloes, whose combined mass is less than 2 percent of that of the host halo. This is not a fair assessment of the impact of environment, and explains why Mao et al. obtained a sHOD that is close to Poissonian for large $\langle N \rangle$.

5 THE MOST MASSIVE SATELLITES OF MILKY WAY-SIZE HALOES

The HOD of massive subhaloes takes central stage in the too-big-to-fail problem (e.g., Boylan-Kolchin et al. 2011; Garrison-Kimmel et al. 2014b, Cautun et al. 2014, Jiang & van den Bosch 2015) and provides one of the most stringent tests of the ΛCDM paradigm. In this section, we adopt the cosmological parameters of the Bolshoi simulation, and use our semi-analytical model combined with data on the most massive satellite galaxies of the Milky-Way, to constrain the mass and formation redshift of the Milky-Way’s host halo (see Cautun et al. 2014 for a similar approach based on the MS-II simulation).

More specifically, we construct 500,000 realizations of host haloes with mass uniformly distributed in the interval $[10^{11.1}, 10^{12.3}]h^{-1}M_\odot$, and select the realizations that match one or more of the following three aspects of the satellite occupation statistics of the Milky Way:

- (i) There are three satellites with $v_{\max} \gtrsim 30 \text{ km s}^{-1}$.
- (ii) There are two Magellanic Cloud analogues, which have $v_{\max} \gtrsim 60 \text{ km s}^{-1}$.

- (iii) There are no less than two Magellanic Cloud analogues and no more than three satellites with $v_{\max} \gtrsim 30 \text{ km s}^{-1}$.

The last condition reflects the v_{\max} ‘gap’ of the Milky Way satellites, in keeping with Cautun et al. (2014) and Jiang & van den Bosch (2015). The main panels of Fig.11 plot the joint distributions of host halo mass and formation redshift for haloes that meet the aforementioned occupation conditions. The side panels show the marginalized distributions for haloes that match the corresponding occupation condition (solid lines), and compare them to the unconstrained distributions for all the 500,000 haloes (dashed lines). Any difference between the solid line and the dashed line reflects the constraint due to the occupation condition.

As shown in the left-hand panel of Fig. 11, Condition (i) favors a relatively low Milky Way mass, with the marginalized distribution peaking at $M_{12} \equiv M_0/10^{12} h^{-1}M_\odot \simeq 0.55$, and $0.2 < M_{12} < 1.3$ at 90% confidence. Condition (i), however, puts no constraint on halo formation time, as the z_f distribution is almost identical to that for all the 500,000 haloes. Over the whole mass range explored here, the fraction of haloes that meet Condition (i) is 12.1%. Condition (ii) favors a much higher Milky Way mass, with $M_{12} > 0.6$ at 90% confidence. The existence of two Magellanic Clouds results in a slight preference of younger haloes, with $0.25 < z_f < 1.4$ at 90% confidence, compared to $0.4 < z_f < 1.82$ for the full sample of 500,000 haloes. Overall, $\sim 7.4\%$ of the haloes in the sample have two Magellanic Cloud-sized satellites, consistent with the result of Liu et al. (2011). Finally, Condition (iii) largely recovers the lower Milky Way mass of Condition (i), while maintaining the preference for a late formation time. The preferred halo mass is at $M_{12} \simeq 0.6$, with $0.25 < M_{12} < 1.4$ and $0.1 < z_f < 1.4$ at 90% confidence. Only 0.66% of all the haloes have a gap feature as required by Condition (iii), consistent with the results of Cautun et al. (2014) and Jiang & van den Bosch (2015).

6 SUMMARY

We have used a combination of N -body simulations and a semi-analytical model to study the statistics of dark matter substructure. In particular, we focused on the halo-to-halo variance of the subhalo mass fraction (f_{sub}) and the detailed shape of the subhalo occupation distribution, and examined in detail how these two aspects of subhalo statistics depend on the formation redshift of the host halo. Our results can be summarized as follows.

- Subhalo disruption is omnipresent in N -body simulations. Based on our semi-analytical model, which is calibrated to match disruption statistics in the Bolshoi simulation, only $\sim 40\%$ (10%) of subhaloes with $m_{\text{acc}} > 10^{-4}M_0$ accreted at $z_{\text{acc}} = 1$ (2) survive to the present. More massive subhaloes are more likely to disrupt, and as many as 80% (95%) of all subhaloes with $m_{\text{acc}} > 0.01M_0$ ($m_{\text{acc}} > 0.1M_0$) have been disrupted since $z_{\text{acc}} = 1$. Roughly 20% of subhaloes with $m_{\text{acc}} > 10^{-4}M_0$ disrupt during their first orbital period. This fraction increases to 30% and 60% for subhaloes with $0.01 \geq m_{\text{acc}} > 0.1M_0$, and $m_{\text{acc}} \geq 0.1M_0$, respectively.
- The average mass fraction of first order subhaloes, $\langle f_{\text{sub}}(> 10^{-4}M_0) \rangle$, scales with host halo mass in a

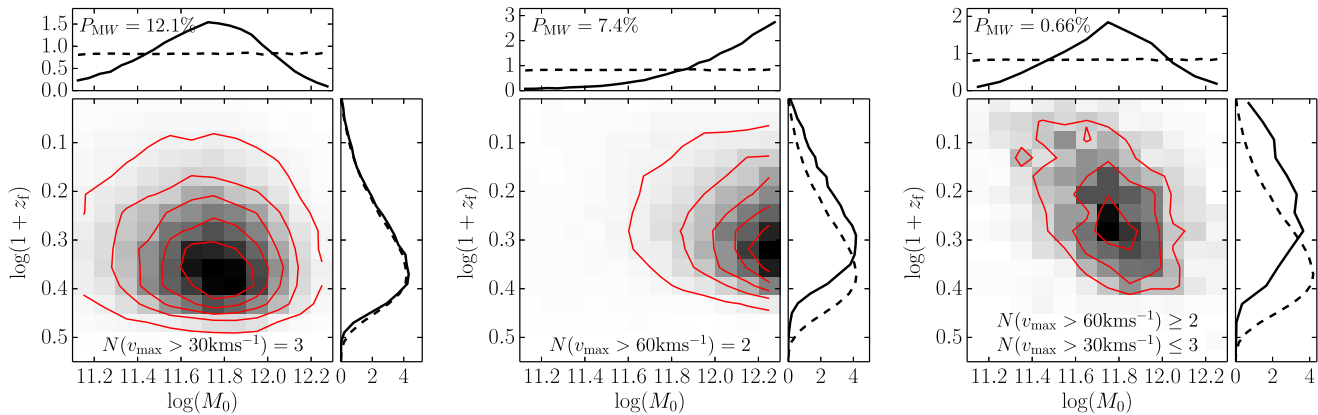


Figure 11. The joint distribution of halo mass and formation redshift for haloes with exactly 3 massive satellites with $V_{\max} > 30 \text{ km s}^{-1}$ (left-hand panel), 2 Magellanic Cloud-analogs with $V_{\max} > 60 \text{ km s}^{-1}$ (middle panel), and with the combined requirement that there are no less than 2 Magellanic Cloud-analogs and no more than 3 massive satellites (right-hand panel). Results are based 500,000 model realizations of host haloes with mass uniformly distributed over the range $M_0 = 10^{11.7 \pm 0.6} h^{-1} M_\odot$. The side panels show the marginalized distributions of host halo mass (up) and formation redshift (side), with solid lines indicating the distributions for haloes that match the required occupation condition, and dashed lines representing the unconstrained distribution for all 500,000 host haloes. The P_{MW} value printed in the upper left corner of each panel indicates the fraction of all host haloes that meet the corresponding occupation condition.

way that is well approximated by $\log\langle f_{\text{sub}} \rangle = -1.12 + 0.12 \log(M_0/10^{12} h^{-1} M_\odot)$. The mass fraction in second-order subhaloes (i.e., sub-subhaloes) is roughly $\sim 10\%$ lower and well approximated by $\log\langle f_{\text{sub}} \rangle = -2.26 + 0.17 \log(M_0/10^{12} h^{-1} M_\odot)$. The halo mass dependence of $\langle f_{\text{sub}} \rangle$ is the outcome of the competition between the accretion of new subhaloes and the evolution of existing ones, and therefore closely related to halo formation redshift. To good approximation $\log\langle f_{\text{sub}} \rangle = a + b \log z_f$ with $(a, b) = (-0.48, -2.1)$ and $(-1.2, -4.0)$ for first- and second-order subhaloes, respectively. Most importantly, at fixed z_f , the average mass fraction is almost independent of M_0 .

- Recently, weak and strong lensing measurements have put constraints on the subhalo mass fraction in the Coma cluster (Okabe et al. 2014) and in a sample of 11 early-type galaxies from the SLACS survey (Vegetti et al. 2014). We find that, in both cases, the lensing measurements are substantially higher than the median model prediction. However, since the halo-to-halo variance is large, we find that the results fall within the 95 percentiles predicted for a Λ CDM cosmology. We caution, though, that the model is calibrated against dark matter-only simulations. Baryonic processes may affect the global subhalo mass fraction, as well as the radial distribution of subhaloes, especially in the central regions of host halos. If baryonic processes have a tendency to *lower* the amount of substructure in the central regions, as suggested by several recent studies (Despali & Vegetti 2016; Fiacconi et al. 2016; Zhu et al. 2016), the lensing measurements are likely to be in tension with Λ CDM predictions. While detailed hydrodynamical simulations are required for a fair assessment, our results at least highlight the importance of properly accounting for the halo-to-halo variance.

- In agreement with numerous previous studies (e.g., Boylan-Kolchin et al. 2010; Busha et al. 2011; Wu et al. 2013), we find that the subhalo occupation distribution (sHOD), $P(N|M_0)$, is super-Poissonian whenever $\langle N \rangle \gtrsim 2$. However, we also find $P(N|M_0)$ to be clearly sub-Poissonian

when $\langle N \rangle$ is small, a trend that had been hinted at in previous studies (e.g., Kravtsov et al. 2004, BK10), but not discussed in any detail. The sub-Poissonity is stronger if subhaloes are selected by m_{acc} or v_{acc} rather than by their present mass or v_{max} . Based on these findings, we present fitting function (Eq.16) for the halo-to-halo scatter $\sigma = \sqrt{\text{Var}(N)}$, as a function $\langle N \rangle$. We caution that there is a hint that different simulations do not converge regarding the deviations from Poissonity, with higher-resolution simulations resulting in a sHOD that is closer to a Poisson distribution (at $\langle N \rangle \gg 1$).

- The 1-halo term of the galaxy two-point correlation function, or equivalently the galaxy power spectrum, depends on the number of satellite pairs $\langle N(N-1) | M_0 \rangle = \alpha^2(M_0) \langle N | M_0 \rangle$. Here $\alpha(M_0)$ simply expresses the relation between the first and second moments of the halo occupation distribution, $P(N|M_0)$. It is common to assume that $P(N|M_0)$ is a Poisson distribution, so that $\alpha(M_0) = 1.0$. However, using our simulation results we show that $\alpha(M_0)$ transits from ~ 1.02 at large $\langle N \rangle$ to smaller than unity at $\langle N \rangle \lesssim 2$. We demonstrate that ignoring this non-Poissonity results in systematic errors in the galaxy-power spectrum (and thus also in the corresponding two-point correlation function) of up to ~ 3 percent, and with a complicated scale- and luminosity-dependence. Although small, such errors are a serious impediment for using galaxy clustering to do precision (i.e. percent-level) cosmology.

- At fixed halo mass, earlier-forming haloes exhibit subhalo occupation statistics that are closer to Poissonian than for their later-forming counterparts. This suggests that the non-Poissonity of subhalo occupation statistics is imprinted at accretion (i.e., in the mass assembly of the host halo), and that subsequent dynamical evolution processes (tidal stripping and heating) drive the occupation statistics to Poissonian.

- We find no evidence to support the claim by Mao et al. 2015 that the super-Poissonian nature of subhalo occupation statistics arises purely from halo-to-halo variance in

formation histories. In particular, we find that the sHOD at fixed halo mass and fixed formation redshift (a proxy for formation history) is not Poissonian, contrary to the model proposed by Mao et al. . Although selecting subhaloes based on both mass and formation redshift slightly reduces the super-Poissonity at large $\langle N \rangle$, it increases the level of sub-Poissonity at small $\langle N \rangle$. We argue that the Poissonian results obtained by Mao et al. (2015) arise from randomizing a too small fraction (less than 2 percent by mass) of the host halo's Lagrangian volume.

- The abundance and v_{\max} distribution of massive satellites only puts loose constraints on the mass and formation redshift of the host halo. In the case of the Milky Way, the requirement that there are three massive satellites with $v_{\max} \gtrsim 30 \text{ km s}^{-1}$ favors a halo mass of $M_0 \sim 10^{11.7 \pm 0.4} h^{-1} M_{\odot}$ (90% CL) but has little to no constraining power regarding its formation redshift. The presence of two Magellanic Clouds favors a high Milky Way halo mass, $M_0 \gtrsim 10^{11.8} h^{-1} M_{\odot}$ (90% CL), and a relatively late formation redshift. Combining these constraints, and demanding a 'gap' in the v_{\max} distribution between that of the SMC and the third largest satellite galaxy, favors a low-mass, late-forming halo, with $0.25 < M_0 / (10^{12} h^{-1} M_{\odot}) < 1.4$ and $0.1 < z_f < 1.4$, both at 90% confidence.

ACKNOWLEDGMENTS

We are grateful to Yao-Yuan Mao and Andrew Hearin for valuable discussions, to Heidi Wu for sharing her results from the Rhapsody simulations, to all the people responsible for the Bolshoi, MultiDark, and ELVIS simulations for making their halo catalogs publicly available, and to the organizers and attendees of the Lorentz Center workshop on 'Dark Matter on the Smallest Scales', for creating a productive environment that had an important impact on this study. FvdB is supported by the Klaus Tschira Foundation and by the US National Science Foundation through grant AST 1516962.

REFERENCES

- Anderhalden D., Diemand J., 2013, JCAP, 4, 9
- Auger M. W., Treu T., Bolton A. S., Gavazzi R., Koopmans L. V. E., Marshall P. J., Bundy K., Moustakas L. A., 2009, ApJ, 705, 1099
- Behroozi P. S., Wechsler R. H., Wu H.-Y., Busha M. T., Klypin A. A., Primack J. R., 2013a, ApJ, 763, 18
- Behroozi P. S., Wechsler R. H., Wu, H.-Y., 2013b, ApJ, 762, 109
- Benson A. J., Baugh C. M., Cole S., Frenk C. S., Lacey C. G., 2000, MNRAS, 316, 107
- Berlind A. A., Weinberg D. H., 2002, ApJ, 575, 587
- Berlind A. A., Weinberg D. H., Benson A. J., Baugh C. M., Cole S., Davé R., Frenk C. S., Jenkins A., et al. , 2003, ApJ, 593, 1
- Bolton A. S., Burles S., Koopmans L. V. E., Treu T., Moustakas L. A., 2006, ApJ, 638, 703
- Boylan-Kolchin M., Springel V., White S.D.M., Jenkins A., 2010, MNRAS, 406, 896 [BK10]
- Boylan-Kolchin M., Bullock J. S., Kaplinghat M., 2011, MNRAS, 415, L40
- Bose S., Hellwing W. A., Frenk C. S., Jenkins A., Lovell M. R., Helly J. C., Li B., Gao L., 2016, preprint (arXiv:1604.07409)
- Bryan G. L., Norman M. L., 1998, ApJ, 495, 80
- Busha M.T., Wechsler R.H., Behroozi P.S., Gerke B.F., Klypin A.A., Primack J.R., 2011, ApJ, 743, 117
- Cacciato M., van den Bosch F. C., More S., Mo H., Yang X., 2013, MNRAS, 430, 767
- Calore F., Cholis I., Weniger C., 2015, JCAP, 1503, 38
- Cautun M., Frenk C. S., van de Weygaert R., Hellwing W. A., Jones B. J. T., 2014, MNRAS, 445, 2049
- Cooray A., Sheth R., 2002, PhR, 372, 1
- Correa C. A., Wyithe J. S. B., Schaye J., Duffy A. R., 2015, MNRAS, 452, 1217
- Dalal N., Kochanek C. S., 2002, ApJ, 572, 25
- De Lucia G., Kauffmann G., Springel V., White S. D. M., Lanzoni B., Stoehr F., Tormen G., Yoshida N., 2004, MNRAS, 348, 333
- Despali G., Vegetti S., 2016, preprint (arXiv:1608.06938)
- Dooley G. A., Griffen B. F., Zukin P., Ji A. P., Vogelsberger M., Hernquist L. E., Frebel A., 2014, ApJ, 786, 50
- Fiacconi D., Madau P., Potter D., Stadel J., 2016, MNRAS, 824, 144
- Gao L., Springel V., White S. D. M., 2005, MNRAS, 363, L66
- Gao L., White S. D. M., 2007, MNRAS, 377, L5
- Gao L., Navarro J.F., Frenk C.S., Jenkins A., Springel V., White S.D.M., 2012, MNRAS, 425, 2169
- Garrison-Kimmel S., Boylan-Kolchin M., Bullock J. S., Lee K., 2014a, MNRAS, 438, 2578
- Garrison-Kimmel S., Boylan-Kolchin M., Bullock J. S., Kirby E. N., 2014, MNRAS, 444, 222
- Ghigna S., Moore B., Governato F., Lake G., Quinn T., Stadel J., 1998, MNRAS, 300, 146
- Giocoli C., Tormen G., Sheth R. K., van den Bosch F. C., 2010a, MNRAS, 404, 502
- Giocoli C., Bartelmann M., Sheth R. K., Cacciato M., 2010b, MNRAS, 408, 300
- Golse G., Kneib J.-P., 2002, A&A, 390, 821
- Han J., Cole S., Frenk C. S., Jing Y., 2016, MNRAS, 457, 1208
- Hearin A.P., Behroozi P.S., van den Bosch F.C., 2016, MNRAS, 461, 2135
- Hezaveh Y. D., Dalal N., Marrone D. P., Mao Y.-Y., Morningstar W., Wen D., Blandford R. D., Carlstrom J. E., et al. , 2016, ApJ, 823, 37
- Jiang F., van den Bosch F. C., 2014, MNRAS, 440, 193
- Jiang F., van den Bosch F. C., 2015, MNRAS, 453, 3575
- Jiang F., van den Bosch F. C., 2016, MNRAS, 458, 2848 [Paper I]
- Klypin A., Gottlöber S., Kravtsov A.V., Khokhlov A.M., 1999, ApJ, 516, 530
- Klypin A., Trujillo-Gomez S., Primack J. R., 2011, ApJ, 740, 102
- Koopmans L. V. E., 2005, MNRAS, 363, 1136
- Kravtsov A. V., Klypin A. A., Khokhlov A. M., 1997, ApJS, 111, 73
- Kravtsov A. V., Berlind A. A., Wechsler R. H., Klypin A. A., Gottlöber S., Allgood B., Primack J. R., 2004, ApJ, 609, 35
- Ludlow A. D., Navarro J. F., Boylan-Kolchin M., Bett P. E., Angulo R. E., Li Ming., White S. D. M., Frenk C., Springel V., 2013, MNRAS, 432, 1103L
- Liu L., Gerke B. F., Wechsler R. H., Behroozi P. S., Busha M. T., 2011, ApJ, 733, 62L
- Macciò A. V., Dutton A. A., van den Bosch F. C., 2008, MNRAS, 391, 1940
- Mao Y.-Y., Williamson M., Wechsler R. H., 2015, ApJ, 810, 21
- McBride J. Fakhouri O., Ma C.-P., 2009, MNRAS, 398, 1858
- Moore B., Katz N., Lake G., 1996, ApJ, 457, 455
- Moster B. P., Naab T., White S. D. M., 2013, MNRAS, 428, 3121
- Navarro J.F., Frenk C.S., White S.D.M., 1997, ApJ, 490, 493
- Neistein E., Dekel A., 2008, MNRAS, 383, 615
- Neto A. F., Gao L., Bett P., Cole S., Navarro J. F., Frenk C. S., White S. D. M., Springel V., et al. , 2007, MNRAS, 381, 1450

- Nierenberg A. M., Treu T., Wright S. A., Fassnacht C. D., Auger M. W., 2014, *MNRAS*, 42, 2434
- Okabe N., Okura Y., Futamase T., 2010, *ApJ*, 713, 291
- Okabe N., Futamase T., Kajisawa M., Kuroshima R., 2014, *ApJ*, 784, 90
- Parkinson H., Cole S., Helly J., 2008, *MNRAS*, 383, 557
- Peñarrubia J., Benson A. J., Walker M. G., Gilmore G., McConnachie A. W., Mayer L., 2010, *MNRAS*, 406, 1290
- Porciani C., Magliocchetti M., Norberg P., 2004, *MNRAS*, 355, 1010
- Prada F., Klypin A.A., Cuesta A.J., Betancort-Rijo J.E., Primack J., 2012, *MNRAS*, 423, 3018
- Purcell C.W., Zentner A.R., 2012, *JCAP*, 12, 7
- Scoccimarro R., Sheth R. K., Hui L., Jain B., 2001, *ApJ*, 546, 20
- Seljak U., 2000, *MNRAS*, 318, 203
- Shaw L. D., Weller J., Ostriker J. P., Bode P., 2006, *ApJ*, 646, 815
- Springel V., White M., Hernquist L., 2001, *MNRAS*, 549, 681
- Springel V., Wang J., Vogelsberger M., Ludlow A., Jenkins A., Helmi A., Navarro J. F., Frenk C. S., White S. D. M., 2008, *MNRAS*, 391, 1685
- Taylor J. E., Babul A., 2004, *MNRAS*, 348, 811
- Tinker J. L., Kravtsov A. V., Klypin A., Abazajian K., Warren M., Yepes G., Gottlöber S., Holz D. E., 2008, *ApJ*, 688, 709
- Tinker J. L., Robertson B. E., Kravtsov A. V., Klypin A., Warren M. S., Yepes G., Gottlöber S., 2010, *ApJ*, 724, 878
- Tormen G., Bouchet F.R., White S.D.M., 1997, *MNRAS*, 286, 865
- van den Bosch F.C., Tormen G., Giocoli C., 2005, *MNRAS*, 359, 1029
- van den Bosch F. C., More S., Cacciato M., Mo H., Yang X., 2013, *MNRAS*, 430, 725
- van den Bosch F. C., Jiang F., Hearin A., Campbell D., Watson D., Padmanabhan N., 2014, *MNRAS*, 445, 1713
- van den Bosch F. C., Jiang F., 2016, *MNRAS*, 458, 2870 [Paper II]
- van den Bosch F. C., Jiang F., Campbell D., Behroozi P., 2016, *MNRAS*, 455, 158
- Vegetti S., Koopmans L. V. E., 2009, *MNRAS*, 400, 1583
- Vegetti S., Koopmans L. V. E., Bolton A., Treu T., Gavazzi, R., 2010, *MNRAS*, 408, 1969
- Vegetti S., Lagattuta D.J., McKean J.P., Auger M.W., Fassnacht C.D., Koopmans L.V.E., 2012, *Nature*, 481, 341
- Vegetti S., Koopmans L. V. E., Auger M. W., Treu T., Bolton A. S., 2014, *MNRAS*, 442, 2017
- Wechsler R.H., Bullock J.S., Primack J.R., Kravtsov A.V., Dekel A., 2002, *ApJ*, 568, 52
- Wechsler R. H., Zentner A. R., Bullock James. S., Kravtsov A. V., Allgood B., 2006, *ApJ*, 652, 71
- Wu H.-Y., Hahn O., Wechsler R. H., Behroozi P. S., Mao Y.-Y., 2013, *ApJ*, 767, 23
- Xu D., Sluse D., Gao L., Wang J., Frenk C., Mao S., Schneider P., Springel V., 2015, *MNRAS*, 447, 3189
- Yang X., Mo H. J., van den Bosch F. C., 2003, *MNRAS*, 339, 1057
- Zhao D. H., Jing Y. P., Mo H. J., Borner G., 2009, *ApJ*, 707, 354
- Zentner A.R., Berlind A.A., Bullock J.S., Kravtsov A.V., Wechsler R.H., 2005, *ApJ*, 624, 505
- Zentner A. R., Hearin A. P., van den Bosch F. C., 2014, *MNRAS*, 443, 3044
- Zheng Z., Berlind A. A., Weinberg D. H., Benson A. J., Baugh C. M., Cole S.; Davé R., Frenk C. S. et al. , 2005, *ApJ*, 633, 791
- Zhu Q., Marinacci F., Maji M., Li Y., Springel V., Hernquist L., 2016, *MNRAS*, 458, 1559